

# Downscaling precipitation over High Mountain Asia using Multi-Fidelity Gaussian Processes: Improved estimates from ERA5

Kenza Tazi<sup>1,2</sup>, Andrew Orr<sup>1</sup>, Javier Hernandez-González<sup>3</sup>, Scott Hosking<sup>1,4</sup>, and Richard E. Turner<sup>2</sup>

<sup>1</sup>British Antarctic Survey, Cambridge, UK

<sup>2</sup>Department of Engineering, University of Cambridge, Cambridge, UK

<sup>3</sup>Microsoft Research, Cambridge, UK

<sup>4</sup>The Alan Turing Institute, London, UK

**Correspondence:** Kenza Tazi (kt484@cam.ac.uk)

**Abstract.** The rivers of High Mountain Asia provide freshwater to around 2-1.9 billion people. However, precipitation, the main driver of river flow, is still poorly understood due to limited direct-in situ measurements in this area. Existing tools to interpolate these measurements or downscale and bias-correct precipitation models have several limitations. To overcome these challenges, this paper uses a probabilistic machine learning approach called Multi-Fidelity Gaussian Processes (MFGPs) to downscale ERA5 climate reanalysis. The method is first validated by downscaling ERA5 precipitation data over data-rich Europe and then data-sparse Upper-upper Beas and Sutlej River Basins-basins in the Himalayas. We find that MFGPs are simpler to implement and more applicable to smaller datasets than other state-of-the-art machine learning models-methods. MFGPs are also able to quantify and narrow the uncertainty associated with the precipitation estimates, which is especially needed over ungauged areas, and can be used to estimate the likelihood of extreme events that lead to floods or droughts. Over the Upper-upper Beas and Sutlej River Basins-basins, the precipitation estimates from the MFGP model are similar to or more accurate than available gridded precipitation products (APHRODITE, TRMM, CRU TS, bias-corrected WRF). The MFGP model and APHRODITE annual mean precipitation estimates generally agree with each other for this region with the MFGP model predicting slightly higher average precipitation and variance. However, more significant spatial deviations between the MFGP model and APHRODITE over this region appear during the summer monsoon. The MFGP model also presents a more effective resolution, generating more structure at finer spatial scales than ERA5 and APHRODITE. MFGP precipitation estimates for the Upper-upper Beas and Sutlej Basins-basins between 1980 and 2012 at a 0.0625° resolution (approx. 9-7 km) are jointly published with this paper.

## 1 Introduction

High Mountain Asia underpins the water security of around 1.9 billion people, supplying them with fresh water for agriculture, energy, industry and domestic usage via Asia's largest rivers (Wester et al., 2019; Immerzeel et al., 2020; Orr et al., 2022). In this area, precipitation drives river flow either directly through rain or, indirectly, by depositing snow reserves that are eventually released through glacier and snow melt (Immerzeel et al., 2020). Precipitation over High Mountain Asia is mainly influenced by

two large scale atmospheric patterns: the Indian ~~summer monsoon and the western disturbances~~Summer Monsoon and Western Disturbances, which dominate in the boreal winter (Bookhagen and Burbank, 2010; Palazzi et al., 2013; Dimri et al., 2015).

25 On a local scale, precipitation over High Mountain Asia is characterised by large variances across relatively small distances of 1 to 10 km due to the region's complex topography (Anders et al., 2006; Bookhagen and Burbank, 2006; Karki et al., 2017; Bookhagen and Burbank, 2010; Sigdel and Ma, 2017; Orr et al., 2017; Bannister et al., 2019). However, the spatiotemporal distribution of precipitation in this area is comparatively poorly understood (Singh et al., 2015; Dahri et al., 2021a; Orr et al., 2022).

30 Knowledge of precipitation patterns in High Mountain Asia is principally constrained by limited observations. Only a small number of *in situ* precipitation observations exist in this region, with most gauge stations placed in unrepresentative locations (below 2000 m a.s.l.) (Winiger et al., 2005; Salzmann et al., 2014; Immerzeel et al., 2015; Duan et al., 2015; Bhardwaj et al., 2017; Krishnan et al., 2019). Indirect observations through satellites are available but struggle to capture the distribution differences between valleys and ridges, as well as short-lived extreme events. Furthermore, satellites often confuse precipita-  
35 tion with ice and snow at the surface level. This leads to remote sensing products generally underestimating precipitation in mountainous areas (Yin et al., 2008; Andermann et al., 2011). These obstacles mean that many physical relationships, such as between precipitation rates and elevation, are not well understood in High Mountain Asia (Dahri et al., 2016). This in turn adversely affects tools to interpolate or combine precipitation measurements to create gridded precipitation products (Meng et al., 2014; Bhardwaj et al., 2017; Hussain et al., 2017; Ji et al., 2020). As a result, ~~interpolated~~interpolation-based products  
40 such as APHRODITE (Yatagai et al., 2012) tend to underestimate precipitation at high altitudes (Immerzeel et al., 2015; Li et al., 2017). Furthermore, such gridded products often have no uncertainty estimates.

In addition to ~~interpolated~~interpolation-based products, outputs from regional climate models (RCMs) can also be used to estimate precipitation over High Mountain Asia (Maussion et al., 2014; Norris et al., 2017, 2019; Orr et al., 2017; Norris et al., 2020). However, these physical models are computationally expensive, lack error estimates, generate large model-dependent  
45 uncertainty (Hawkins and Sutton, 2009), and are generally not well-optimised for mountainous regions (Cannon et al., 2017; Norris et al., 2017, 2019; Orr et al., 2017). For example, the ensemble of RCMs from the Coordinated Regional Climate Downscaling Experiment (CORDEX) for South Asia regularly overestimates historical precipitation over High Mountain Asia by over 100% for both winter and summer (Sanjay et al., 2017). RCM precipitation outputs therefore typically need to be bias-corrected before use in this region (Maussion et al., 2014; Collier and Immerzeel, 2015; Bannister et al., 2019; Potter  
50 et al., 2022).

Climate reanalysis products offer an alternative for estimating precipitation by combining ~~output~~outputs from short-range forecast models with observations through data assimilation. These products often struggle to accurately represent precipita-  
tion over data-sparse areas or times, including High Mountain Asia (Dahri et al., 2016; Palazzi et al., 2013). ERA5 climate reanalysis (Hersbach et al., 2020), although generally exhibiting a wet bias for High Mountain Asia, provides relatively ac-  
55 curate precipitation estimates in terms of amounts, seasonality, and variability, from daily to multi-annual scale compared to other reanalysis and RCM products (Chen et al., 2021; Kumar et al., 2021).

Altogether, precipitation products over High Mountain Asia are often contradictory and lack consensus (Palazzi et al., 2013; Bannister et al., 2019). These discrepancies further complicate our understanding and leave room for doubt in any given prediction or estimate. As precipitation is the main driver of hydrological models (Meng et al., 2014; Remesan and Holman, 2015; Wulf et al., 2016), improving precipitation estimates is key to a better representation of the spatial and temporal dynamics of hydrological processes. These improved estimates can in turn help us better understand, predict and mitigate extreme events such as droughts, floods and landslides (Ji et al., 2020; Dahri et al., 2021b; Schreiner-McGraw and Ajami, 2022). ~~Finally, current precipitation estimates~~ Present day precipitation estimates also underpin the accuracy of future precipitation predictions (Panday et al., 2015; Sanjay et al., 2017).

Traditional and state-of-the-art statistical downscaling techniques are used to address these problems but present their own issues. ~~These methods~~ For High Mountain Asia, downscaling models often assume simplistic relationships, e.g. a linear correlation between precipitation and elevation, and focus on single basins (Dahri et al., 2016; Bannister et al., 2019; Libertino et al., 2018). New research is making the most of machine learning tools to downscale precipitation products (Yadav et al., 2024; Gerlitz et al., 2014), allowing researchers to model more complex spatiotemporal precipitation distributions and generate products over larger areas and longer time periods (Ahmed et al., 2020; Ning et al., 2016; Mei et al., 2020; Sun et al., 2022). These studies are also using machine learning corrected precipitation directly as inputs to hydrological models (Sun et al., 2022; Xiang et al., 2024) and applying machine learning methods to merge precipitation data from multiple sources to improve prediction robustness in ungauged areas (Lyu and Yong, 2024; Xiang et al., 2024; Zhang et al., 2021).

However, these downscaling methods generally struggle to simultaneously solve the following problems: 1) capturing extreme values and spatiotemporal structure, 2) generalising to multiple locations, 3) predicting at arbitrary locations, 4) overcoming gridding biases and 5) working effectively with sparse and ‘small’ datasets (King et al., 2013; Maraun and Widmann, 2018; Baño-Medina et al., 2020; ?; Andersson et al., 2023). We propose Multi-Fidelity Gaussian Processes (MFGPs) as an alternative to other statistical downscaling and bias-correction methods. Using MFGPs, ~~multiple precipitation~~ precipitation data from multiple sources can be combined to overcome these challenges and increase the accuracy and effective resolution of precipitation predictions over topographically complex areas, especially over ungauged locations. Most importantly, the probabilistic nature of MFGPs provides a principled way of quantifying uncertainty and the likelihood of extreme precipitation events.

This study focuses on applying MFGPs to downscale ERA5 monthly precipitation estimates in the data-sparse Upper-upper Beas and Sutlej River ~~Basins~~ basins in the Himalayas, ~~which~~ The Beas and Sutlej are two main tributaries of the Indus River. The study area, shown in Figure 1, serves as a pilot study for High Mountain Asia. The paper is structured as follows. ~~MFGPs and~~ Gaussian Processes (GPs) and MFGPs are first introduced in Section 2. The methodology and datasets used are presented in Section 3. The MFGPs are then evaluated by downscaling ERA5 precipitation, first over a data-rich region (Europe) and then over a subset of the Upper-upper Beas and Sutlej ~~Basins~~ basins, in Section 4. The MFGP framework is then applied to the whole of the Upper-upper Beas and Sutlej ~~Basins~~ basins and compared with precipitation dataset benchmarks including APHRODITE in Section 5. Finally, the limitations of this approach and further work are discussed in Section 6.

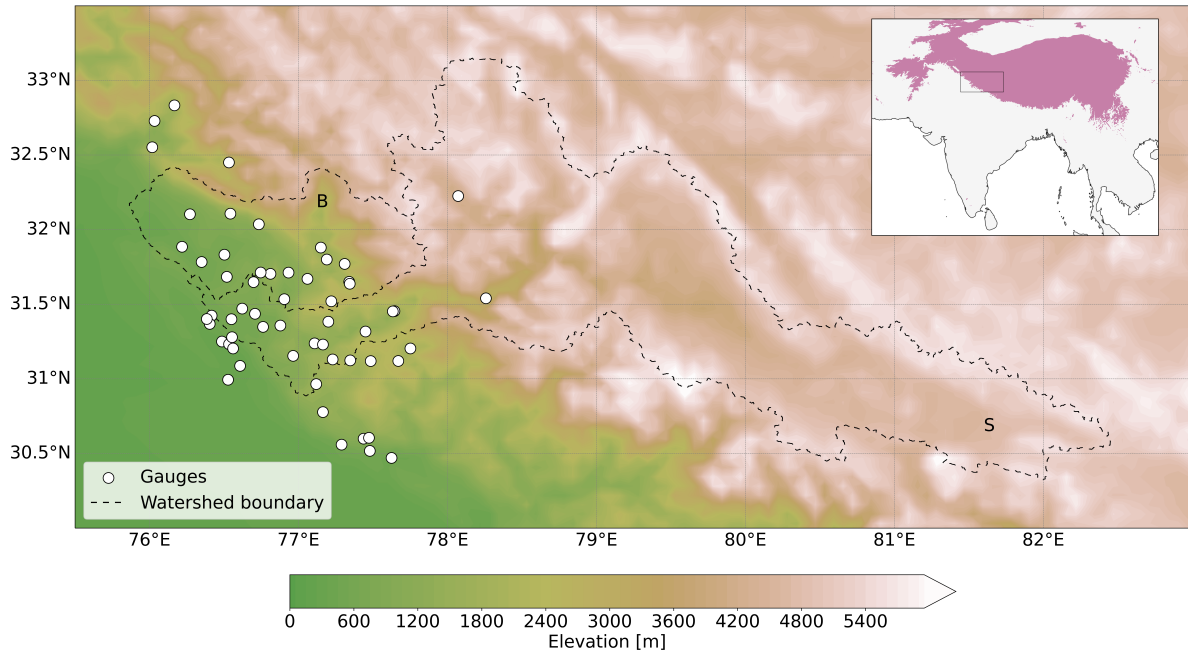


**Figure 1.** Elevation map of the Upper-upper Beas and Sutlej River Basins-basins with gauge locations represented by white circles. The dashed line represents the watershed boundaries, with the letter ‘B’ denoting the Upper-upper Beas River-Basin-basin and ‘S’ the Upper upper Sutlej River-Basin-basin. Only three gauge stations are located above 2000 m. The inset shows the watersheds’ location with respect to High Mountain Asia, with areas above 2000 m a.s.l. highlighted in purple.

## 2 Multi-Fidelity Gaussian Processes

### 2.1 Gaussian Processes

Consider the set of observations  $\mathbf{x}_i, y_i$  with  $i = \{1, \dots, N\}$ ,  $\mathbf{x}_i \in \mathbb{R}^D$  and  $y_i \in \mathbb{R}$  where  $N$  is the number of data points and  $D$  the number of observation dimensions. In this paper,  $\mathbf{x}_i$  represents a vector with the date, coordinates and elevation of the observation and  $y_i$  is its monthly precipitation value. These observations are generated by a function  $f$ :

$$y_i = f(\mathbf{x}_i) + \epsilon_i \quad (1)$$

where  $\epsilon_i$  is the noise term and is assumed to be distributed normally with a mean of zero and standard deviation  $\sigma_n$ , i.e.,  $\epsilon_i \sim \mathcal{N}(0; \sigma_n^2)$ . The function  $f$  can be modelled with a Gaussian Process (GP). We refer the reader to Rasmussen et al. (2006) for an introduction to GPs and follow their notation in this presentation. A GP is a stochastic process where any finite collection of its random variables is distributed according to a multivariate normal distribution. Similarly to a multivariate normal distribution, a GP is defined by a mean function  $\mu(\mathbf{x}, \boldsymbol{\theta}_\mu)$  and covariance or kernel function  $k(\mathbf{x}, \mathbf{x}', \boldsymbol{\theta}_k)$ :

$$f(\mathbf{x}) \sim GP(\mu(\mathbf{x}, \boldsymbol{\theta}_\mu), k(\mathbf{x}, \mathbf{x}', \boldsymbol{\theta}_k)) \quad (2)$$

where  $x$  is the input vector to predict at,  $x'$  is another arbitrary input location, and  $\theta_\mu$  and  $\theta_k$  represent the hyperparameters of the mean and covariance functions respectively. The hyperparameters are the parameters of the model that can either be set manually or optimised. Going forward the hyperparameters will be referred to jointly as  $\theta$ . The covariance function  $k(x, x', \theta_k)$  strongly underpins the GP model. ~~The covariance function~~ It captures the correlation of the outputs given the inputs and encodes encoding properties such as smoothness and periodicity. If the covariance function is stationary, the correlation depends only on the distance between  $x$  and  $x'$ .

As the output of a GP for a single point is a probability distribution, the GP output over many points can be interpreted as a probability distribution over functions. Predictions at new input locations can therefore be calculated using Bayes' theorem. This is also known as the model being 'fit' to the data or 'training' the model with the data. If  $A$  represents ~~all the values of the GP~~ the GP's functions and  $B$  the data, Bayesian inference can be written as:

$$p(A|B, C) = \frac{p(A|C)p(B|A, C)}{p(B|C)} \quad \text{where} \quad A = f(\cdot), \quad B = \{x_i, y_i\}_{i=1}^N, \quad C = \theta \quad (3)$$

where  $p(A|B, C)$  is the probability distribution of  $A$  conditional on  $B$  and  $C$  with all other distributions defined analogously. This can be seen as the system  $A$  being updated using new information  $B$ .  $p(A|C)$  is therefore known as the prior distribution and  $p(A|B, C)$  as the posterior distribution. ~~The full-posterior distribution is especially relevant when estimating the likelihood of extreme values and~~ is therefore a principled way to define the uncertainty of the model ~~and is therefore estimating the probabilities of extreme values.~~  $p(B|A, C)$  is the probability of the observations  $B$  occurring given the state of system  $A$  with hyperparameters  $C$  and is known as the likelihood.  $p(B|C)$  is known as the marginal likelihood and is the probability density of the observations given the hyperparameters. This distribution is calculated by integrating or 'marginalising' over all the values of  $f$ , i.e. going from  $p(B|A, C)$  to  $p(B|C)$ .

GPs therefore are non-parametric. Instead of optimising over finite set of parameters, e.g. weights of a random forest or neural network, GPs are optimised over functions. Consequently, GPs are more expressive in how they fit the data compared to traditional regression or classification models, i.e. they can be used to model complex relationships between the data. GPs are also more robust to overfitting because rather than optimise a specific function, it integrates over all potential ones (Rasmussen et al., 2006).

Practically, the mean function  $\mu(x, \theta_\mu)$ , the covariance function  $k(x, x', \theta_k)$  and the prior distribution are built from a set of standard functions that encode different assumptions. In particular, the covariance matrix is usually designed by multiplying or adding standard kernel functions together (Rasmussen et al., 2006; Duvenaud et al., 2013). The covariance function makes GPs well suited for highly-correlated geophysical datasets and quantifying uncertainty in absence of data. However these benefits come at a cost, the computational complexity of GPs scales cubically with the number of data points. This scaling is an issue in large data regimes but can be addressed by low-rank approximations and inducing points (Liu et al., 2020; Tazi et al., 2023).

## 2.2 Multi-Fidelity Gaussian Processes

The fidelity of a dataset can be defined as a combination of the data’s precision and accuracy. The most accurate set of observations with the highest resolution are referred to as the high-fidelity-high-fidelity data. Less accurate and coarse observations or simulation data are denoted as low-fidelity-low-fidelity data. In many cases, high-fidelity-high-fidelity observations can be expensive to produce whereas low-fidelity-low-fidelity observations are usually more inexpensive and therefore more numerous. A multi-fidelity model combines low-fidelity-low-fidelity datasets with the more accurate, but limited, observations in order to predict the high-fidelity-high-fidelity output more effectively. Datasets of different fidelities can be combined using GPs, where the output of a first GP is used as the input to the next and so forth. For a Multi-Fidelity Gaussian Process (MFGP), each layer of the model represents a different level of fidelity, starting from the lowest and moving towards the highest fidelity.

Consider  $s$  fidelity levels each corresponding to different datasets, e.g., climate reanalysis, gauge station measurements, etc. Each fidelity is made up of observations  $\mathbf{Y}_t$  at locations  $\mathbf{X}_t \subseteq \mathbb{R}^D$  where  $t = 1, \dots, s$ . The observations  $\mathbf{Y}_s$  denote the outputs of the most accurate and expensive function to evaluate  $f_s$ , whereas  $\mathbf{Y}_1$  is the outputs of the cheapest and least accurate function  $f_1$ . The highest-fidelity-highest-fidelity data are assumed to be sampled from the ‘true’ distribution of the target function. The observations at level  $t$  can be generated by a function  $f_t$ :

$$Y_{t,i} = f_t(\mathbf{X}_{t,i}) + \epsilon_{t,i} \quad (4)$$

where  $\epsilon_{t,i}$  is the noise term.

One choice for this function is given by Le Gratiet and Garnier (2014). The approach requires two assumptions. First, the relationship between the fidelities is assumed to be linear. Second, the model follows strict hierarchical sampling rules where the fidelity levels have nested training sets. The high-fidelity-high-fidelity locations must be contained within the domain of the lower-fidelity-lower-fidelity. The lowest-fidelity-lower-fidelity data must therefore have the largest domain, the second fidelity must have the second-largest domain and so forth. From these assumptions, the function  $f_t$  is defined as:

$$f_t(\mathbf{X}_t) = \rho_t f_{t-1}(\mathbf{X}_t) + f_{\text{err}}(\mathbf{X}_t). \quad (5)$$

The function  $f_t$  is the high-fidelity-high-fidelity GP as modelled by the scaled sum of two functions  $f_{t-1}$  and  $f_{\text{err}}$ . The function  $f_{t-1}$  is a GP modelling the outputs of the lower-fidelity-lower-fidelity function and is scaled by  $\rho_t$ , a scalar indicating the magnitude of the correlation to the high-fidelity-high-fidelity data. The function  $f_{\text{err}}$  is another GP that models the bias between the two fidelity levels. The scaling factor  $\rho_t$  is defined as:

$$\rho_t(\mathbf{X}_t) = \frac{\text{cov}(f_t(\mathbf{X}_t), f_{t-1}(\mathbf{X}_t))}{\text{var}(f_{t-1}(\mathbf{X}_t))} \quad (6)$$

where cov is the covariance and var is the variance. Model inference, including the propagation of the mean and standard deviation through different fidelity levels, is discussed in Appendix A. Figure 2 illustrates the MFGP framework for a pedagogical example using two toy datasets.

### 3 Method and datasets

#### 3.1 Method overview

165 In this study we use the MFGP framework to combine two datasets of different fidelities: ~~high fidelity~~ high-fidelity gauge measurements, which are accurate but sparse, and climate reanalysis data, which are complete but more biased. In this way, the MFGP is applied to downscale and bias-correct monthly reanalysis precipitation ~~ERA5 reanalysis~~-data using precipitation gauge measurements. Time, latitude, longitude and elevation are used as input variables. The datasets used to train the MFGPs and make predictions from the model are described in Section 3.2. The MFGP framework is validated ~~over-using subsets of~~ European station data and then ~~a subset of the Upper~~ upper Beas and Sutlej gauge data. MFGP is first applied to Europe in order to ascertain the performance of the model on an area with less sparse gauge data and more homogeneous spatial distribution of precipitation before applying it to the more challenging Upper-upper Beas and Sutlej regions. A MFGP model is then trained using all the gauges in Upper-upper Beas and Sutlej ~~Basins~~ basins and compared to other benchmark datasets. The benchmark datasets, their advantages and their limitations are presented in Section 3.3.

#### 175 3.2 Training and prediction datasets

The datasets used to train the MFGP model include the VALUE gauge measurements over Europe (~~high fidelity~~ high-fidelity), the Beas and Sutlej gauge measurements (~~high fidelity~~ high-fidelity), and ERA5 (~~low fidelity~~ low-fidelity). The ~~resampled GMTED2010-dataset~~ digital elevation model is also presented and is used ~~as inputs~~ to make the high resolution precipitation estimates over the Upper-upper Beas and Sutlej ~~Basins~~ basins.

180 **VALUE gauge measurements.** The European station measurements are taken from the VALUE downscaling experiment (Gutiérrez et al., 2019). The dataset features daily precipitation at 86 stations across Europe between 1979 and 2019. These stations are representative of different climatic regimes over the European continent including mountainous environments. The daily data is re-sampled to a monthly temporal resolution.

**Beas and Sutlej gauge measurements.** The Upper-upper Beas and Sutlej ~~Basins-were~~ basins are chosen as the study ~~regions~~ region as they offer comparatively data-rich locations for High Mountain Asia (Wulf et al., 2016; Bannister et al., 2019). The dataset from Bannister et al. (2019) with additional quality control is used. The dataset is made up of 58 stations (~~with 46 in the~~ Upper-within the upper Beas and Sutlej ~~Basins~~ basins) ~~with basins and~~ measurements between January 1980 and April 2013. The 23 stations run by the Bhakra Beas Management Board measure rainfall and snow water equivalent. The remaining 35 stations are run by the Indian Meteorological Department and only record rainfall. This is not problematic as all these stations are below the snow line in this area (Lund et al., 2020). The precipitation observations are daily but have missing values with gaps of several years for most locations. The stations cover less than half of the study area as seen in Figure 1. With station altitudes ranging from 284 m to 3639 m a.s.l. and a median altitude of 935 m a.s.l., most stations are not representative of the ~~area which has combined watersheds which together have~~ a median elevation of approximately 4700 m a.s.l. The data is ~~converted resampled~~ converted resampled from daily to monthly averages.

195 **ERA5.** The ~~5th~~<sup>5<sup>th</sup></sup> ECMWF Reanalysis (ERA5) (Hersbach et al., 2020) is used ~~as the final model input to train the low fidelity GPs of the MFGP model.~~ ERA5 runs from 1950 to the present day over 0.25° ~~by 0.25°~~ grid and assimilates data from a large number of sources. ERA5's global spatial coverage and long temporal range make it an attractive dataset. It is also easily accessible and straightforward to update. The monthly total precipitation variable is used in the following experiments. Elevation values are derived from ERA5's geopotential variable.

200 **GMTED2010.** The 2010 global multi-resolution terrain elevation data (GMTED2010) is a digital elevation model computed from 11 satellite data sources (Danielson and Gesch, 2011). The model provides elevation products at three separate resolutions of 30 arc-seconds (approx. 1 km), 15 arc-seconds (approx. 500 m), and 7.5 arc-seconds (approx. 250 m) with global land coverage from 84° N to 56° S for most products. In this paper, ~~an~~<sup>a</sup> resampled version of GMTED2010 at 0.0625° resolution from the European Space Agency's Tropospheric Monitoring Instrument team (TROPOMI, 2019).

### 205 3.3 Benchmark datasets

Precipitation estimates using the MFGP framework are compared against the following precipitation benchmark datasets: bias-corrected WRF, APHRODITE, TRMM, and CRU TS.

**Bias-corrected WRF.** The bias-corrected WRF output is a product that was specifically developed for the ~~Upper-upper~~ Beas and Sutlej ~~Basins-basins~~ by Bannister et al. (2019). Here, version 3.8.1 of the WRF model (Skamarock et al., 2008) was used  
210 to dynamically downscale ERA-Interim reanalysis data (Dee et al., 2011) to a grid spacing of 5 km from 1980 to 2012. The precipitation outputs from the model were then bias-corrected using the *in situ* observations described above, using a power transformation method proposed by Leander and Buishand (2007).

**APHRODITE.** The second benchmark is the Asian Precipitation-Highly Resolved Observational Data Integration Towards Evaluation of water resources or ~~APHRODITE (Yatagai et al., 2012)~~<sup>(APHRODITE Yatagai et al., 2012)</sup>. APHRODITE data  
215 ranges from 1951 to 2015 with a maximum spatial resolution of ~~0.25°~~. The interpolation scheme uses nearby precipitation gauges, slope and a correlation distance lookup table. In the paper, we use the APHRO\_V1101 gridded precipitation product which was specifically developed for monsoon Asia. Overall, APHRODITE has one of the best spatiotemporal coverage of gridded precipitation products over High Mountain Asia. It is also one of the most studied and accurate products for the region (Dimri, 2021). However, the interpolation scheme underestimates precipitation at high altitudes and suffers from spatially het-  
220 erogeneous biases when compared to *in situ* observations. These biases pose critical limitations for high-precision hydrological studies (Ji et al., 2020; Bhardwaj et al., 2017; Hussain et al., 2017).

**TRMM.** The Tropical Rainfall Measuring Mission (TRMM) is a satellite mission that was launched at the end of 1997 and remained active until 2014. TRMM provides good spatial coverage over High Mountain Asia, although several studies have shown that ~~its relatively coarse 0.25° resolution~~<sup>the relatively coarse resolution of its products</sup> is unable to capture distribution  
225 differences between valleys and ridges (Shukla et al., 2019; Andermann et al., 2011; Yin et al., 2008). Additionally, its relatively poor temporal coverage (only a few overpasses per day) also contributes to extreme precipitation events not being captured.



Here we use TRMM\_3B43 data, which is a monthly 0.25° resolution Level 3 precipitation product where radar and radiometer measurements have been converted to precipitation values and the results have been calibrated against ground measurements (Japan Aerospace Exploration Agency, 2018). However, the calibration sites are not in High Mountain Asia.

230 **CRU TS**. The final benchmark is the high-resolution Climatic Research Unit global climate Time Series dataset (~~CRU TS v4.05~~) developed at the University of East Anglia (Harris et al., 2020) (CRU TS v4.05 Harris et al., 2020). This gridded dataset uses an angular-distance weighting interpolation of *in situ* observations between 1901 and 2020. This resulting product has a 0.5° resolution and was chosen as a baseline ~~, given it's~~ given its coarser resolution and global scope.

## 4 Model validation

### 235 4.1 Experimental setup

#### 4.1.1 Validation ~~schemes~~scheme

The MFGP model is evaluated from 2000 and 2004 over both Europe and the Upper-upper Beas and Sutlej Basinsbasins. This time period represents the time with the largest number of active stations in the Upper-upper Beas and Sutlej Basinsbasins. For both regions, the MFGP model is tested using fivefold cross-validation. This means the data are first separated into five groups  
240 or folds and five separate models are trained on different permutations of four groups and tested on the fifth. Cross-validation is therefore a useful way to estimate how the model will perform in practice when it is asked to predict at arbitrary locations far way from its training distribution. The groups are determined via k-means clustering on the station locations. To make the cross-validation clusters even in size, only the seven closest stations to the cluster centres are kept. The cluster downsizing also increases the spatial independence between folds. The folds for both regions are shown in Figure 3.

245 Different variants of this cross-validation method are used to evaluate the MFGP model. First, we setup a ‘data-rich’ experiment over Europe. In this case, all the available stations except the test fold stations are used to train the model. For example, when evaluating the model on ~~fold~~Fold 1 (Figure 3 ~~(a)~~a), blue markers), the model is trained on the other folds and the grey stations. In this setting, the model therefore has access to more data including data that are climatically similar to where the model is evaluated. We then modify the experiment to create a ‘~~data-sparsedata-sparse~~’ setting over Europe. In this case, we train only  
250 the data in the training folds and test on the excluded group. The ‘~~data-sparsedata-sparse~~’ scheme is repeated for the evaluation over the Upper-upper Beas and Sutlej Basinsbasins. This progressive reduction in data should help compare the impact of the data sparsity on the MFGP model against that of complex spatiotemporal precipitation distribution in the Upper-upper Beas and Sutlej Basinsbasins.

#### 4.1.2 Data ~~transformations~~transformation

255 The probability distribution function of monthly precipitation is not Gaussian but usually follows a log-normal distribution. However, as the GP posterior distribution is constrained to be Gaussiannormal, making the marginal distribution more normal

can [therefore](#) help with inference. For this reason, the precipitation data are transformed using a Box-Cox function fit to the [low-fidelity-low-fidelity](#) ERA5 data:

$$y_i(\lambda) = \begin{cases} \frac{y_i^\lambda - 1}{\lambda}, & \text{if } \lambda \neq 0 \\ \log y_i, & \text{if } \lambda = 0 \end{cases} \quad (7)$$

260 where  $y_i$  is the  $i^{\text{th}}$  observation and is assumed to be positive and  $\lambda$  is the scaling factor. The input features are standardised by subtracting the mean and dividing standard deviation of the training set before they are passed to the models. This is also known as z-scoring and generally improves inference.

### 4.1.3 Kernel design

The MFGP kernels are specified to be Matérn  $\frac{5}{2}$  functions defined as:

$$265 \quad k_{\text{Mat}}(\mathbf{x}, \mathbf{x}') = \frac{\sigma^2}{\Gamma(\nu)2^{\nu-1}} \left( \frac{\sqrt{2\nu}}{l} |\mathbf{x} - \mathbf{x}'| \right)^\nu K_\nu \left( \frac{\sqrt{2\nu}}{l} \right) \quad (8)$$

where  $\nu = 5/2$ ,  $\sigma^2$  is the variance parameter,  $l$  the lengthscale parameter,  $\Gamma$  is the gamma function, and  $K_\nu$  is the modified Bessel function of the second kind. The Matérn  $\frac{5}{2}$  function provides samples that are more faithful to real physical processes compared to the default squared exponential kernel. The samples are twice differentiable, i.e. not completely smooth, thus allowing for more abrupt changes in the modelled variable. The Matérn  $\frac{5}{2}$  kernel performed better than the squared exponential kernel for  
270 both the Europe and [Upper-upper](#) Beas and Sutlej [Basin-basin](#) experiments (not shown).

### 4.1.4 Machine learning baselines

The performance of the MFGP is compared to [linear regression model trained on ERA5 data](#), [several baseline models](#). [We would like to establish that using both low and high-fidelity data improve models that use just one or the other. In order to do this, we implement](#) a GP fit to ERA5 [data](#) using a Matérn  $\frac{5}{2}$  kernel, and a GP fit to the station data using a Matérn  $\frac{5}{2}$  kernel.  
275 The GP fit to ERA5 using a Matérn  $\frac{5}{2}$  is equivalent to the MFGP [low-fidelity-low-fidelity](#) output. Finally, the MFGP is also compared to a GP fit on the station data with the custom kernel design. The custom kernel is defined as:

$$k = k_{\text{Mat52}}(\mathbf{t}) \cdot k_{\text{Per}}(\mathbf{t}) + k_{\text{Mat52-ARD}}(\text{lat}, \text{lon}, \text{elevation}) \quad (9)$$

where  $k_{\text{Mat52}}$  is the Matérn  $\frac{5}{2}$  kernel,  $k_{\text{Per}}$  is the periodic kernel, and  $k_{\text{Mat52-ARD}}$  is the Matérn  $\frac{5}{2}$  exponential kernel with Automatic Relevance Determination (ARD) (MacKay, 1994). ARD allows the kernel parameters to vary between input dimensions.  
280 The periodic kernel is defined as:

$$k_{\text{Per}}(\mathbf{x}, \mathbf{x}') = \sigma^2 \exp \left( -\frac{2 \sin(2\pi|\mathbf{x} - \mathbf{x}'|/p)}{l^2} \right) \quad (10)$$

where  $p$  is the period parameter,  $\sigma^2$  is the variance parameter and  $l$  the lengthscale parameter.<sup>1</sup> A similar kernel design to Equation 9 was used over the ~~Upper Indus Basin~~ upper Indus basin with ERA5 precipitation by Lalchand et al. (2022) and was found to perform as well as more complex non-stationary kernel functions. The kernel design was formulated following the framework proposed Tazi et al. (2023) where statistical analysis of the precipitation data and domain knowledge, such as the periodic temporal patterns and the strong influence of elevation, were combined to create a kernel that is predictive without being unnecessarily complex.

~~Finally, we investigate current state-of-the-art downscaling models:~~ Additionally, the MFGP model is compared to other models commonly used to interpolate or downscale precipitation for small datasets. We implement three non-probabilistic models including linear interpolation and random forest and support vector regression downscaling where ERA5 precipitation is directly used as a high-fidelity precipitation predictor. We also compare the MFGP with a strong alternative probabilistic model, namely a Convolutional Conditional Neural Processes-Process (ConvCNP)(Gordon et al., 2019; ?) and Convolutional Gaussian Neural Processes (ConvGNP) (Markou et al., 2022; Andersson et al., 2023). These models offer similar advantages to the MFGP model, including: capturing extreme values and spatiotemporal structure, generalising to multiple locations, predicting at arbitrary locations and overcoming gridding biases. However, these neural networks require a large number of datapoints to be trained adequately, and therefore training them on the same amount of data as the MFGP model did not allow them to converge to any physically sensible outputs. We therefore omit these results in the following sections but present the code to implement the models in the supplementary material. Although these models contextualise the MFGP performance, they do not contribute towards the main goal of demonstrating how the uncertainty can be narrowed by incorporating multiple data sources. For this reason, these models are discussed in Section 6.

#### 4.1.5 Performance metrics

Several metrics are used to evaluate the models. The root mean square error (RMSE) is calculated for the validation sets as well as their 5<sup>th</sup> percentile and 95<sup>th</sup> percentile values to evaluate how well the model is capturing extremes. The RMSE is ~~chosen as a performance metric as it is~~ more robust to outliers than the mean absolute error or the bias. We also calculate the coefficient of determination ( $R^2$ ) to understand how much of the variance in the data is represented by the model. These metrics are chosen in part for their broad usage across both machine learning and environmental science fields. The mean log loss (MLL) computes average negative logarithm of the posterior likelihood of all validation points. This metric ~~therefore~~ is a measure of the model confidence and the quality of its uncertainty predictions. The MLL is more suited to probabilistic methods than RMSE or  $R^2$ . All the metrics are defined in Appendix B.

---

<sup>1</sup>Although  $\sigma^2$  and  $l$  serve similar purposes to the parameters of the Matérn  $\frac{1}{2}$  kernel shown in Equation 8, they are actually distinct variables and optimised separately.

## 310 4.2 Validation over Europe

The MFGP framework is first applied to a ‘data-rich’ setting over Europe. Table 1 shows the performance of the MFGP with respect to other simpler GP models ~~and linear regression~~. Of these methods, the GP with the custom kernel extrapolating only from gauges yields the poorest results ~~-This with a negative  $R^2$  indicating that the model is predicting worse than the precipitation mean. This poor predictive skill~~ is expected as the custom kernel is designed to model precipitation over the Western Himalayas and not Europe. By contrast, precipitation estimates from the ~~linear regression model and the~~ GPs with the Matérn kernels provide better results. In particular, applying a GP fit to ERA5 data at every station location gives even better estimates compared to a GP fit to the station data, including the best estimates for 95<sup>th</sup> percentile RMSE ( $2.58 \pm 1.11$  mm/day). However, the MFGP model gives the best overall results with lowest mean and 5<sup>th</sup> percentile RMSE ( $1.06 \pm 0.42$  mm/day and  $0.51 \pm 0.20$  mm/day respectively), the highest  $R^2$  ( $0.65 \pm 0.09$  mm/day), and the ~~highest lowest~~ MLL ( $0.89 \pm 0.20$ ).

Model	Training features	RMSE [mm/day]	RMSE5 [mm/day]	RMSE95 [mm/day]	$R^2$	MLL
MFGP	gauges + ERA5	<b><math>1.06 \pm 0.42</math></b>	<b><math>0.51 \pm 0.20</math></b>	$2.72 \pm 1.54$	<b><math>0.65 \pm 0.09</math></b>	<b><math>0.89 \pm 0.20</math></b>
GP <sub>Mat52</sub>	ERA5	$1.16 \pm 0.43$	$0.52 \pm 0.25$	<b><math>2.58 \pm 1.11</math></b>	$0.57 \pm 0.13$	$(1.87 \pm 0.71) 10^7$
GP <sub>custom</sub>	gauges	$1.91 \pm 0.69$	$1.60 \pm 0.22$	$5.58 \pm 2.06$	$-0.14 \pm 0.23$	$1.57 \pm 0.19$
GP <sub>Mat52</sub>	gauges	$1.21 \pm 0.45$	$0.59 \pm 0.29$	$2.85 \pm 1.17$	$0.55 \pm 0.14$	$1.94 \pm 0.36$

**Table 1.** Comparison of model performance metrics for the ‘data-rich’ setup over Europe. The models include the MFGP, a GP using the custom kernel, and a GP using a Matérn  $\frac{5}{2}$  kernel with ARD. The metrics include the average RMSE (RMSE), the 5<sup>th</sup> percentile RMSE (RMSE5), the 95<sup>th</sup> percentile RMSE (RMSE95), the  $R^2$ , and the MLL. The training features represent inputs used to train the models. The errors represent the standard deviation across the validation folds. Bolded values show the best model performance for a given metric.

320 The experiment is then repeated for the ‘~~data-sparse data-sparse~~’ setting. Table 2 shows the performance metrics for this setup. Despite a small decrease in performance compared to the ‘~~data-rich data-rich~~’ experiment shown in Table 1, the MFGP model is still able to combine the two datasets to improve predictions. The other baselines also show a generalised decreases in skill but their ranking is unaffected.

Model	Training features	RMSE [mm/day]	RMSE5 [mm/day]	RMSE95 [mm/day]	$R^2$	MLL
MFGP	gauges + ERA5	<b><math>1.13 \pm 0.47</math></b>	<b><math>0.57 \pm 0.23</math></b>	$3.02 \pm 1.62$	<b><math>0.62 \pm 0.11</math></b>	<b><math>0.90 \pm 0.20</math></b>
GP <sub>Mat52</sub>	ERA5	$1.21 \pm 0.46$	$0.59 \pm 0.29$	<b><math>2.84 \pm 1.17</math></b>	$0.55 \pm 0.14$	$(18.7 \pm 7.4) 10^6$
GP <sub>custom</sub>	gauges	$2.25 \pm 0.90$	$1.10 \pm 0.60$	$6.51 \pm 2.29$	$-0.57 \pm 0.46$	$1.73 \pm 0.33$
GP <sub>Mat52</sub>	gauges	$2.13 \pm 0.91$	$1.21 \pm 0.48$	$6.29 \pm 2.35$	$-0.39 \pm 0.44$	$1.62 \pm 0.31$

**Table 2.** As Table 1 for the ‘data-sparse’ setup over Europe.

Figure 4 (a) plots the ~~high-fidelity-high-fidelity~~ output as a function of ~~low-fidelity-low-fidelity~~  $R^2$  for the validation locations. The high-fidelity output corresponds to the MFGP fit using both ERA-ERA5 and the gauge data. The ~~low-fidelity-low-fidelity~~ MFGP fit uses on ERA5 only and is equivalent to fitting a simple GP to ERA5 as shown in Table 2. Values above the dashed line show the locations where combining the datasets leads to improved performance. The plot shows that the MFGP improves predictions at most station locations. The largest gains are observed over the European alps (shown in orange). Simultaneously this is also the area, along with the Pyrenees and northern Spain (shown in green) where the model produces the largest errors. Altogether these results show that MFGPs can confidently be applied to more data-sparse locations.

### 4.3 Validation over ~~Upper-upper~~ Beas and Sutlej ~~Basins~~~~basins~~

Table 3 shows the performance of the MFGP with respect to other simpler GP models ~~and linear regression for the Upper-for~~ ~~the upper~~ Beas and Sutlej ~~Basins~~~~basins~~. Overall the performance of the MFGP model and machine learning baselines is worse than over Europe, with all metrics showing a decrease in skill. This can be explained for two reasons. First, ERA5 is more accurate over Europe than the ~~Upper-upper~~ Beas and Sutlej ~~Basins~~ (~~see~~ ~~basins~~ (cf. Tables 2 and 3). Second, the precipitation in the High Mountain Asia presents more extreme seasonal variations, so is harder to predict (see Appendix C). The higher spatial heterogeneity of the precipitation over the ~~Upper-upper~~ Beas and Sutlej ~~Basins~~ ~~basins~~ should not strongly contribute to the performance difference as the ~~scale of the study area is much smaller than that of the European experiment while the number of stations remains the same~~ ~~standardised spatial lengthscales between the European and Himalayan stations are similar~~ (see Appendix C).

~~In particular, the~~ ~~The~~ MFGP's MLL and RMSE metrics suffer the most compared to the European experiments and the GP baselines. The MFGP's RMSE values grow approximately by a factor of 3 and the MLL by a factor of 2. This behaviour could be caused by the specific temporal distribution of precipitation in the ~~Upper-upper~~ Beas and Sutlej. For most of the year, precipitation values stay low but increase dramatically during the ~~summer monsoon~~ ~~Indian Summer Monsoon~~, peaking in June/July. If the model does not predict these extreme values, the MLL and RMSE are heavily penalised. Conversely, the stronger periodicity in the data makes it easier to fit the GP models thus comparatively improving the GP MLL scores and ~~5th~~ ~~5th~~ percentile RMSE. The MFGP still outperforms the GP fit ~~for to~~ ERA5 and the GP ~~extrapolation using~~ ~~extrapolating from~~ the station data only with a mean RMSE ( $3.00 \pm 0.92$  mm/day) and  $R^2$  ( $0.46 \pm 0.11$ ). In this experiment, ~~all the probabilistic models show better performance than the linear regression model on the low fidelity data alone. In particular, the~~ ~~the~~ GP with the custom kernel outperforms the GP with the Matérn kernel suggesting that incorporating domain knowledge becomes more important in this more complex precipitation regime. ~~The experiments were also conducted with all the ERA5 data for the study area (not shown), but showed no significant improvement over using the ERA5 data at the station locations only.~~

Figure 4 (b) plots the ~~high-fidelity-high-fidelity~~  $R^2$  as a function of ~~low-fidelity-low-fidelity~~  $R^2$  for the validation locations across the basins. The figure shows that when the ~~low-fidelity-low-fidelity~~  $R^2$  is already high ( $>0.5$ ), the MFGP improvements are limited. However, when the ~~low-fidelity-low-fidelity~~  $R^2$  is low, the MFGP significantly improves the ~~low-fidelity-low-fidelity~~ fit. The ~~Upper-upper~~ Beas and Sutlej ~~low-fidelity-low-fidelity~~  $R^2$  values also cover a much larger range. Although the MFGP

Model	Training features	RMSE [mm/day]	RMSE5 [mm/day]	RMSE95 [mm/day]	R <sup>2</sup>	MLL
MFGP	gauges + ERA5	<b>3.00±0.92</b>	1.66±0.95	9.62±3.63	<b>0.46±0.11</b>	1.79±0.22
GP <sub>Mat52</sub>	ERA5	3.32±0.79	2.39±1.52	<b>7.56±2.81</b>	0.26±0.32	(11.4±4.8) 10 <sup>7</sup>
GP <sub>custom</sub>	gauges	3.16±1.00	0.99±0.76	10.46±4.33	0.40±0.11	<b>1.67±0.31</b>
GP <sub>Mat52</sub>	gauges	3.24±1.35	<b>0.86±0.56</b>	11.0±5.11	0.38±0.25	1.66±0.32

**Table 3.** As Table 2 for the Upper Beas and Sutlej basins.

improves the ~~low-fidelity-low-fidelity~~ predictions less consistently than over Europe, it makes larger improvements over ERA5 over the ~~Upper-upper~~ Beas and Sutlej basins. In particular, the largest improvements are observed for Fold 4 (shown in red) which has the highest average elevation and is therefore most representative of the basins’ ungauged areas. This result is  
360 therefore encouraging given the paper’s objective to predict in high altitude ungauged locations.

## 5 Application to ~~Upper-upper~~ Beas and Sutlej ~~Basins~~basins

### 5.1 Study area predictions

A MFGP model is now trained using all available station data, including the stations outside of the basins, and ERA5 data over the study area (30° N-33.5° N, 75.5° E-83° E) between 2000 and 2009. This corresponds to the overlapping period  
365 between all the benchmark datasets studied in the following section. Again the precipitation values are transformed and input features are z-scored before they are passed to the model as this improves model inference. Separate models are trained on a yearly basis due to memory and computational constraints. In the Appendix D, we show that, ~~assuming no missing data~~, this does not significantly impact the results of the model performance~~assuming no missing data~~. When training the model across the entirety of both basins, the MFGP ~~high-fidelity-function-high-fidelity~~ GP initially optimised the longitude lengthscale  
370 to a very small value. This produced nonphysical looking results with striations along lines of same longitude. Therefore, Gaussian prior distributions of  $\mathcal{N}(0.1^\circ, 0.01^\circ)$  are set for the longitude and latitude lengthscale parameters such that they would optimise to similar values. This choice is motivated by the expectation that the precipitation lengthscales ~~are-should be~~ similar along these dimensions. The ~~prior parameter~~ values are selected based on the optimised ~~parameters-hyperparameters~~ for the MFGP’s ~~low-fidelity-function-and-the-high-fidelity-values-low-fidelity~~ GP and the ~~high-fidelity hyperparameters~~ from the  
375 MFGP validation experiment. Finally, the GMTED2010 dataset was used (Danielson and Gesch, 2011) ~~as-for~~ the prediction locations ~~and elevations~~. The dataset’s 0.0625° resolution (approx. ~~9-7~~ km) allows the MFGP model to predict at high enough resolution to enable municipal decision making (Rambali, 2020).

The average annual and seasonal precipitation MFGP ~~outputs-predictions~~ are shown in Figure 5. The mean of the MFGP posterior distribution is compared to ERA5 precipitation in the first two rows. The MFGP annual average shows that most of

380 the precipitation is concentrated in the west half of the study area over the Himalayan foothills. During the monsoon season, the MFGP shows an average rainfall reaching 10 mm/day. The monsoon also brings rain to the southeastern side of the ~~Upper Sulej Basin. Although the upper Sulej basin. Although~~ estival precipitation distributions are similar, the highest precipitation values of the MFGP model are shifted ~~to the West in comparison to west relative to~~ ERA5. In the winter months, the variance in precipitation is more attenuated and the distribution centre is shifted to the North East and thus towards higher elevations.

385 In contrast with the ~~Upper Beas Basin upper Beas basin,~~ precipitation over the eastern ~~Upper Sulej Basin shows a proportional relationship upper Sulej basin increases with~~ altitude with valleys showing overall little rain or snowfall (<2 mm/day) across all seasons. These findings qualitatively echo previous studies on the spatiotemporal distribution of precipitation in this area, including the non-stationary and complex pattern of ~~altitudinal precipitation orographic precipitation gradients~~ (Dahri et al., 2016; Bannister et al., 2019).

390 The 95% confidence interval (CI) of MFGP model is also plotted in Figure 5. This metric represents the interval in which 95% of the ~~model MFGP~~ outputs fall into. The CI boundary values therefore show possible extreme precipitation values. The CI is therefore used as a measure of uncertainty. ~~For this investigation, the The~~ most salient characteristic of the CI is that it is large in comparison to the mean of the posterior distribution (, over 45 mm/day for several locations. For both the monsoon and winter seasons the CI is largest in the area around 32°N, 77°E at the western edge of the study area. This ~~is due to a conflict between the~~

395 ~~low and high fidelity function behaviour is linked to conflicting low and high fidelity~~ predictions where ERA5 ~~suggest smaller suggests high~~ precipitation values while the ~~high fidelity high fidelity~~ gauge data suggest the precipitation should be ~~high much smaller~~ at the same location. Conversely, over ungauged areas, the CI remains low. This shows the improved predictive power of combining reanalysis and gauge data ~~in a probabilistic framework.~~

The mean posterior distribution and CI are then combined in a bivariate choropleth map in the bottom row of Figure 5.

400 In general, the CI is expected to increase with higher precipitation values. This plot allows us to identify the regions that have the highest uncertainty output compared to their mean predictions, i.e. a high ‘relative uncertainty’. The east and higher altitude ungauged locations generally have a high relative uncertainty, and areas with a high gauge density have a lower relative uncertainty. However, the choropleth map does exhibit some smaller unexpected features. For example, a high relative uncertainty area in the west of the ~~Upper Beas Basin upper Beas basin~~ (32°N, 76°E) and low relative uncertainty in the southern

405 borders of the ~~Upper Sulej Basin upper Sulej basin~~ that receives more precipitation during the monsoon and winter seasons. Again, this points to the MFGP model successfully capitalising on information from both precipitation datasets.

The effective resolution of the MFGP model is also compared with that of ERA5. Effective resolution refers to the level of detail ~~or structure~~ that can be accurately represented by the model. The effective resolution can be determined through the data’s power spectrum ~~density~~. The power spectrum ~~density~~ shows the amount of the structure present in the dataset for a given

410 wavenumber  $k$  or resolution  $k^{-1}$ . When the ~~power spectrum spectral~~ density is low, it is not contributing structure at that resolution and therefore not representing the physical processes at that scale. To generate the power spectrum ~~density, the, a~~ Fourier transform of the precipitation is calculated for each month over a square area (31°-33° N, 77°-79° E). ~~The To proceed equitably, the~~ ERA5 data is linearly interpolated along ~~it’s its~~ spatial coordinates to the same resolution as the MFGP ~~and both~~

datasets are z-scored. Figure 6 shows the power-spectrum-spectral density  $P$  falls off as a function of the resolution for both  
415 ERA5 and MFGP. Although ERA5 has a native resolution of  $0.25^\circ$  (approx. 31 km), it possesses a relatively small amount of  
structure compared to the MFGP the same resolution. The MFGP model continues to generate more structure at finer scales  
too. This points to the MFGP representing spatial patterns of precipitation better than ERA5.

## 5.2 Comparison with benchmark datasets

To further evaluate the performance of the MFGP model over the Upper-upper Beas and Sutlej Basinsbasins, the benchmark  
420 datasets described in Section 3.3 are now compared to the *in situ* observations between 2000 to 2009. All the available  
station data in the Upper-upper Beas and Sutlej basins (46 of 58 available stations) are used. Nearest neighbour precipitation  
values to the station locations are reported. It is important to note that ~~APHRODITE, CRU and~~ bias-corrected WRF ~~have or~~  
~~have most likely used the~~ has used these gauge measurements in ~~their development.~~ its development. This is also most likely  
the case for APHRODITE and CRU TS. Table 4 compares the performance of the products across the different metrics. As the  
425 MFGP model is trained on all these datapoints, we do not include the model's performance here as to not make an inequitable  
comparison.

APHRODITE outperforms the other products for the mean RMSE ( $2.36 \pm 0.86$  mm/day), 5<sup>th</sup> percentile RMSE ( $0.56 \pm 0.61$   
mm/day) and  $R^2$  ( $0.43 \pm 1.01$ ) metrics. ERA5 has the best 95<sup>th</sup> percentile RMSE ( $6.17 \pm 3.54$  mm/day) but the poorest  
5<sup>th</sup> percentile RMSE ( $0.84 \pm 0.79$  mm/day). For this area, TRMM simultaneously ~~possesses-yields~~  
430 ( $3.99 \pm 1.43$  mm/day) and 95<sup>th</sup> percentile RMSE ( $8.54 \pm 4.02$  mm/day). The results for ERA5 and TRMM match ~~the previous~~  
~~findings~~ previous findings, exhibiting wet and dry biases respectively (Kumar et al., 2021; Chen et al., 2021; Andermann et al.,  
2011; Shukla et al., 2019; Yin et al., 2008). The bias-corrected WRF product has the worst  $R^2$  performance ( $-0.31 \pm 2.80$ ). Over-  
all the table shows that the performance of these models is highly heterogeneous across both basins with all metrics showing  
large standard deviations.

435 From ~~these results~~ Table 4, APHRODITE was determined ~~by the authors~~ to be the most accurate of the benchmarks presented  
in the paper for this region and time period. The differences between APHRODITE and the MFGP output are therefore com-  
pared ~~using annual and seasonal averages in Figure 7~~. The average ~~annual~~ precipitation across the basin for the MFGP output  
and APHRODITE between 2000 and 2009 do not differ much, with a mean and standard deviation of 1.73 mm/day and 2.37  
mm/day respectively for the MFGP model compared to 1.61 mm/day and 2.33 mm/day for APHRODITE. Figure 7 maps  
440 out the annual and seasonal averages. The annual average shows local spatial differences on the order of  $\pm 2.5$  mm/day. How-  
ever ~~the~~ seasonal averages show a much larger differences between the two datasets. In particular, APHRODITE predicts lower  
precipitation values in the northwest corner of the ~~Upper-Beas Basin~~ upper Beas basin ( $-5$  mm/day to  $-8$  mm/day) and higher  
values on southeast side of the ~~Upper-Beas Basin~~ upper Beas basin ( $+2.5$  mm/day to  $+5$  mm/day) during the summer mon-  
soon. These difference are large compared to the values shown in Figure 5. ~~These differences~~ This is also where MFGP places  
445 the most uncertainty in Figure 5. These results, in combination with the spatial differences between the MFGP and ERA5,  
point to an ambiguous spatial representation of peak precipitation values in the Himalayan foothills during the monsoon. In



	Input features	RMSE [mm/day]	RMSE5 [mm/day]	RMSE95 [mm/day]	R <sup>2</sup>
ERA5	multiple <sup>†</sup>	2.83±0.89	0.84±0.79	<b>6.17±3.54</b>	-0.11±1.98
APHRODITE	gauges	<b>2.36±0.86</b>	<b>0.56±0.61</b>	6.45±3.46	<b>0.43±1.01</b>
TRMM	remote sensing	3.99±1.43	0.83±0.76	8.54±4.02	-0.18±0.51
CRU TS	gauges	2.76±1.09	0.62±0.39	7.63±4.23	0.25±1.15
Bias-corrected WRF	gauges + WRF	3.13±0.94	0.73±0.92	7.02±3.34	-0.31±2.80

**Table 4.** RMSE and R<sup>2</sup> values for benchmark datasets over Upper Beas and Sutlej Basins between 2000 and 2010. Only stations located in the basins (46 out of 58) are used to evaluate the datasets. The errors represent the standard deviation across the stations. As some of these benchmarks are or are likely produced using the station data, it is not possible to compare these results with the previous table. Bolded values show the best model performance for a given metric. <sup>†</sup> ERA5 uses only remote sensing data for precipitation measurements but is also constrained using direct measurements for other climatic variables.

the winter, the differences are smaller due to on average lower precipitation rates (between +5 and -1.5 mm/day). During this period, MFGP model predicts lower precipitation estimates at higher altitudes compared to APHRODITE. Finally, the power spectrum **density** for APHRODITE is calculated in Figure 6. The dataset presents a smaller average effective resolution compared to the MFGP and even ERA5.

## 6 Discussion and further work

### 6.1 MFGP **model** extensions

The MFGP model is easily applicable to other watersheds and mountainous regions such as the Andes or European Alps, or to downscale other reanalysis or climate models. The model resolution is also arbitrary and higher resolution results could be generated by using a higher resolution digital elevation model when predicting at new times and locations. This flexibility makes MFGP a powerful tool for hydrological and, more generally, geophysical modelling.

In this paper, we apply a linear setup. ~~It is also was applied.~~ However, it is possible to apply the nonlinear form of the model, known as Nonlinear Auto-Regressive GP (NARGP) (Perdikaris et al., 2017):

$$f_t(\mathbf{X}_t) = g_t(\mathbf{X}_t, f_{t-1}(\mathbf{X}_t)), \quad (11)$$

where  $g_t \sim GP(f_t | \mu_t, k_{t_g}((\mathbf{X}_t, f_{t-1}(\mathbf{X}_t)), (\mathbf{X}'_t, f_{t-1}(\mathbf{X}'_t))); \theta_t)$ . Unlike linear MFGP, NARGP captures a nonlinear relationships between the different fidelities. However, the auto-regressive architecture of the model is also one of its limitations. The model specifies each GP is fitted in an isolated hierarchical manner. This type of inference means the model's complexity is not controlled through Bayesian inference and makes it more susceptible to overfitting. This was found to be true for the precipitation datasets presented in this paper. An alternative could be to implement a Multi-Fidelity Deep Gaussian Process (MFDGP)

465 proposed by Cutajar et al. (2019) where the evaluation at each fidelity level is performed using data ~~at the current level and the~~  
~~previous ones~~from the current and previous fidelity levels. However, the MFDGP method requires the use of inducing points  
which can be hard to initialise without strong machine learning and environmental domain knowledge.

## 6.2 ~~Model~~MFGP validation

### 6.2.1 With respect to GPs

470 In the validation experiments, we use datasets with no or a small number of missing values to compare the performance of the  
model with other methodological benchmarks. In this case, we are only evaluating how well the model extrapolates in space.  
This works in favour of the simple GP model that extrapolates from the ~~high fidelity~~high-fidelity gauge data. However, the  
simple GP's accuracy suffers significantly when extrapolating with respect to time, which is required when making predictions  
for incomplete datasets. This ~~is another point in favour~~behaviour is another advantage of using a multi-fidelity model. The  
475 model validation in this study also highlights the impact of the observation scarcity to model accuracy. Tackling the impact  
of climate change on water scarcity in High Mountain Asia therefore requires more data sharing initiatives and consistent  
investment in weather station maintenance and deployment.

### 6.2.2 With respect to benchmarks

The benchmark datasets are compared on the validation folds in Appendix C. In this experiment, the MFGP model is able  
480 to outperform the other models on some metrics over the data held out from the model (see Section 4.3). In particular, the  
model still scores the best for  $R^2$  (MFGP  $R^2=0.46\pm 0.11$  vs average of  $R^2=0.00$ ) despite most of these datasets being ~~trained~~  
~~on~~produced using these *in situ* observations. This shows that the underlying variations of data are being more accurately  
captured by the MFGP model, even if the amplitude of those variations are captured less precisely (higher RMSE scores). This  
lower precision makes sense as we expect the model to widen ~~it's~~its posterior distribution at locations far from ~~it's~~its training  
485 distribution. Furthermore ~~this~~the MFGP product, unlike previous ones, ~~outputs~~includes principled uncertainty estimates in the  
form of probability distributions. This can allow policymakers to understand the likelihood of worst case scenarios of drought  
or flooding. These ~~uncertainties~~uncertainty distributions can also be directly used to inform the placement of future sensors  
through multi-objective Bayesian optimisation (Daulton et al., 2021, 2020). The MFGP model outputs could for example be  
490 combined with distance from roads and trails as a proxy for accessibility. Together station locations that are both predictive  
and practical could be found. Finally, the model can be easily updated with new station data through online learning, a feature  
which is unique to Bayesian inference (Bui et al., 2017; Lederer et al., 2021).

### 6.2.3 With respect to other machine learning models

The performance of the MFGP model is also contextualised through the implementation of three non-probabilistic baseline  
models and a probabilistic deep learning model. Results and model implementation details are presented in Appendix E.

495 The performance of the linear interpolation model is first assessed. We note that the model presented in this paper is similar to the interpolation scheme used for precipitation in ERA5-Land (Muñoz-Sabater et al., 2021). ERA5-Land is a reanalysis dataset that provides a consistent view of the evolution of land variables at an enhanced spatial resolution of 9 km. This is produced by running a land surface model to regenerate some of the land components of ERA5 climate reanalysis. For atmospheric forcing, it uses ERA5 atmospheric variables including precipitation which are linearly interpolated to the ERA5-Land grid. The linear  
500 interpolation model also includes elevation as a predictor which should allow it to perform better than ERA5-Land especially over mountainous regions.

Overall, linear interpolation performs significantly worse over both Europe and the Beas and Sutlej basins than the MFGP, and even its probabilistic counterpart, the GP fit to ERA5. This can be attributed to the GP's generation of non-linear functions that better capture ERA5's physics and data assimilation.

505 We then contrast the MFGP to random forest and support vector regression. Both random forests (Ho, 1995) and support vector regression (Drucker et al., 1996) have been used extensively to downscale precipitation, including over High Mountain Asia (Sun et al., 2022; Xiang et al., 2024; Ahmed et al., 2020; Yan et al., 2022; Ning et al., 2016; Mei et al., 2020). Both methods work well with small datasets, are non-linear, and, for support vector regression, are kernel-based like GPs.

The random forest and support vector regression models perform similarly to the MFGPs in terms of RMSE/R<sup>2</sup> for the  
510 'data-rich' Europe experiment. However the MFGP performs consistently better for these metrics and is less sensitive to the reduction of data when moving to the 'data-sparse' setup. Over Europe, the random forests are however better at representing extreme values across all the cross validation folds. Over the Beas and Sutlej basins, the MFGP dominates offering more better and more consistent results with the exception of the 5<sup>th</sup> percentile RMSE. The relatively poor performance for the low percentiles values is due to the GP and MFGP models reverting to the observation mean in locations far from the training  
515 distribution where they are uncertain rather than confidently predicting lower values like the non-probabilistic models.

Lastly, ConvCNPs are also implemented for the validation experiments. The ConvCNP model is one member of the neural process model family that has shown state-of-the-art performance in spatiotemporal downscaling tasks (Vaughan et al., 2022; Gordon et al.,  
. Neural processes offer similar advantages to the MFGP in terms of being able to quantify the probability of extreme events, generalise to multiple locations, predict at arbitrary locations, and overcome gridding biases. The results show that these  
520 models overfit these relatively small datasets performing worse than linear regression, in particular, for the Beas and Sutlej experiment. This is not surprising as neural networks generally require a large number of datapoints to be trained adequately. As these models can be used for transfer learning, future work could investigate the using data from other mountainous regions to inform predictions in data-sparse High Mountain Asia. In summary, the MFGPs are best suited to downscaling in the sparse and out-of-distribution settings presented in this paper.

### 525 6.3 Applicability of results

The MFGP model output for 33-year period between 1980 and 2012 over the ~~Upper-upper~~ Beas and Sutlej ~~Basins-basins~~ is made available for scientists, hydrologists and policymakers to perform more thorough research and water security risk assessments (Tazi, 2023). However, there are several limitations to its applicability. A key shortcoming to the results, as with many precipitation product in mountainous areas, is the underestimation of precipitation estimates due to undercatch. This is especially true in exposed areas and where precipitation falls as snow. Implementing the model a year at a time is also problematic. This means the model, at times with fewer observations, cannot leverage the mappings that exist at other times. Furthermore, predictions have been made for a monthly resolution only and ~~could be are~~ inappropriate for hydrological models that usually operate on a daily timescale. These constraints come from the computational ~~constraints-of-the-framework~~complexity of the MFGP. The framework could also be applied across High Mountain Asia but this would also be computationally expensive. These problems could be overcome by applying variational~~and~~, product-of-experts, or low-rank approximations to the MFGP model (~~Titsias, 2009; Wilson and Nickisch, 2015~~)(Tresp, 2000; Titsias, 2009; Wilson and Nickisch, 2015).

## 7 Conclusions

MFGPs are simpler and more accurate than recent ~~state-of-the-art~~state-of-the-art models and traditional techniques for smaller study areas with sparse datasets. The framework offers better mean RMSE and  $R^2$  than the bias-corrected regional climate model output at prediction time. MFGP and APHRODITE perform similarly on average. Contrasting the two products across the basins shows general consensus about the total amount of annual precipitation. However, there are key areas where predictions diverge including over high altitudes in the winter and the north of the ~~Upper-Beas-Basin~~upper Beas basin during the summer monsoon. Furthermore, the MFGP model also provides principled and well-calibrated uncertainty quantification. The model also provides a higher effective spatial resolution, providing more than three times the structure than ERA5 and APHRODITE at a  $0.25^\circ$  resolution. ~~These improvements~~The continued improvements of these estimates will be key factors to improving hydrological modelling and water security policy. Future work could apply the framework across High Mountain Asia, predict precipitation on daily timescale, conduct sensor placement analysis, and implement variational, product-of-experts or low-rank approximations to MFGP framework to improve computational tractability.

*Code and data availability.* The code for this paper is available at: <https://github.com/kenzaxtazi/mfgp>. The MFGP model output between 1980 and 2012 for the upper Beas and Sutlej basin is available at: <https://doi.org/10.5285/b2099787-b57c-44ae-bf42-0d46d9ec87cc>. The ERA5 data is available through the Copernicus Data Store (<https://cds.climate.copernicus.eu/>). The VALUE gauge data is available through the VALUE experiment website (<http://www.value-cost.eu/data>). The GMTED2010 elevation data used is available from the Tropospheric Emission Monitoring Internet Service (<https://www.temis.nl/data/gmted2010/index.php>). The authors of this paper do not have the required permission to make the Beas and Sutlej gauge dataset publicly available and suggest that any readers interested in obtaining it refer to Wulf et al. (2016).

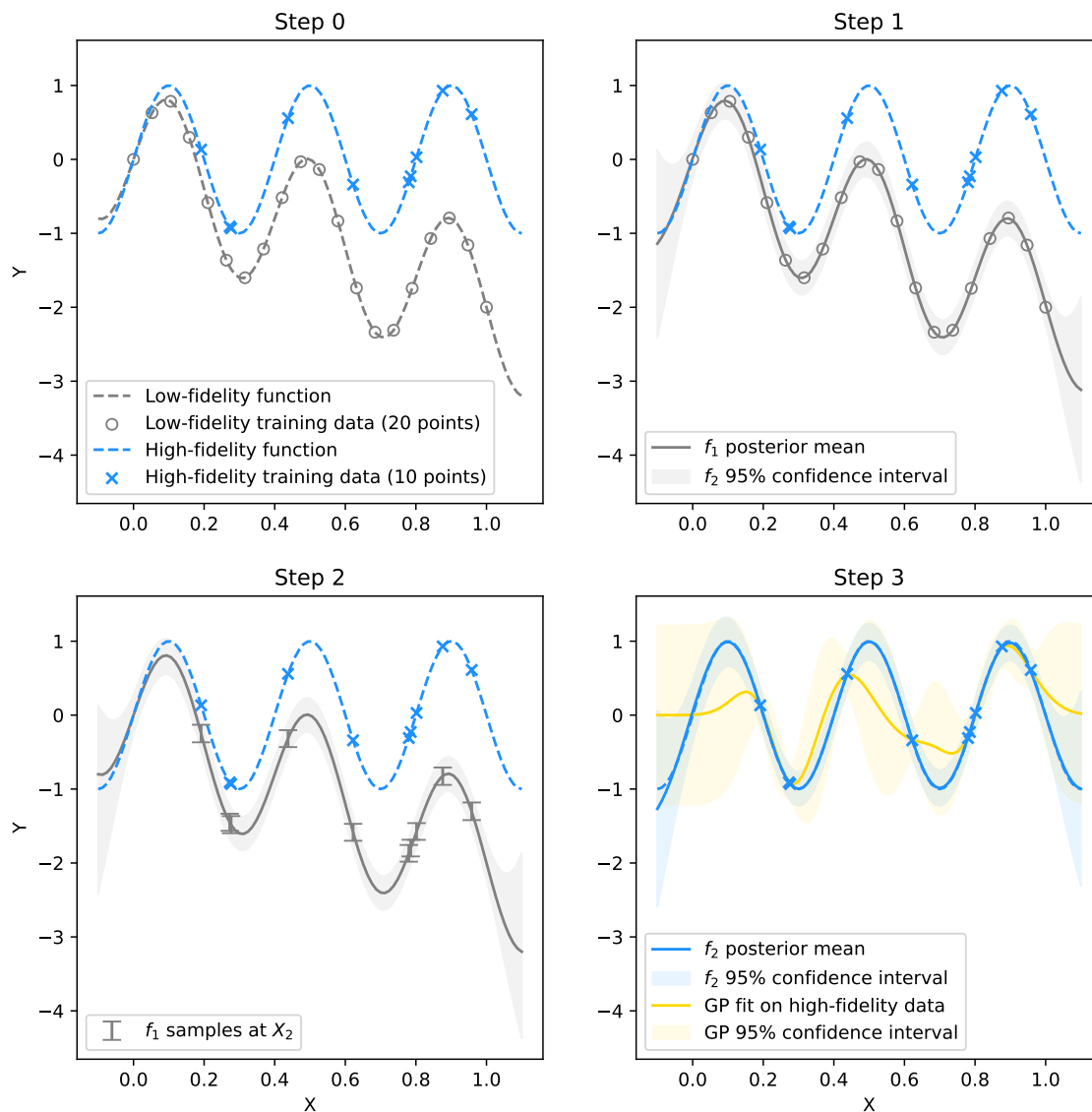


**Figure 2.** One dimensional pedagogical example of a MFGP model. The low-fidelity-first-low-fidelity dataset is first contrasted with the high-fidelity-high-fidelity data (Step 0). The high-fidelity-high-fidelity data is more sparse but has a higher resolution than the low-fidelity-low-fidelity data, and is also nested within the low-fidelity-low-fidelity input domain. The first GP  $f_1$  is constrained by the lowest-fidelity-lowest-fidelity observations  $Y_1(\mathbf{X}_1)$  (Step 1). Function  $f_1$  is visualised through its posterior distribution mean (grey continuous line) and its 95% confidence interval (grey shaded area) and can be used to make predictions at new locations. Samples from  $f_1$  at  $\mathbf{X}_2$  (Step 2) and the observations from the second fidelity  $Y_2(\mathbf{X}_2)$ , are then used as the inputs to the second GP  $f_2$  (Step 3). The final panel also shows the output of simple GP fit to the high-fidelity-high-fidelity data only. The simple GP model fails to capture the underlying high-fidelity-high-fidelity function and produces a more poorly constrained posterior distribution.

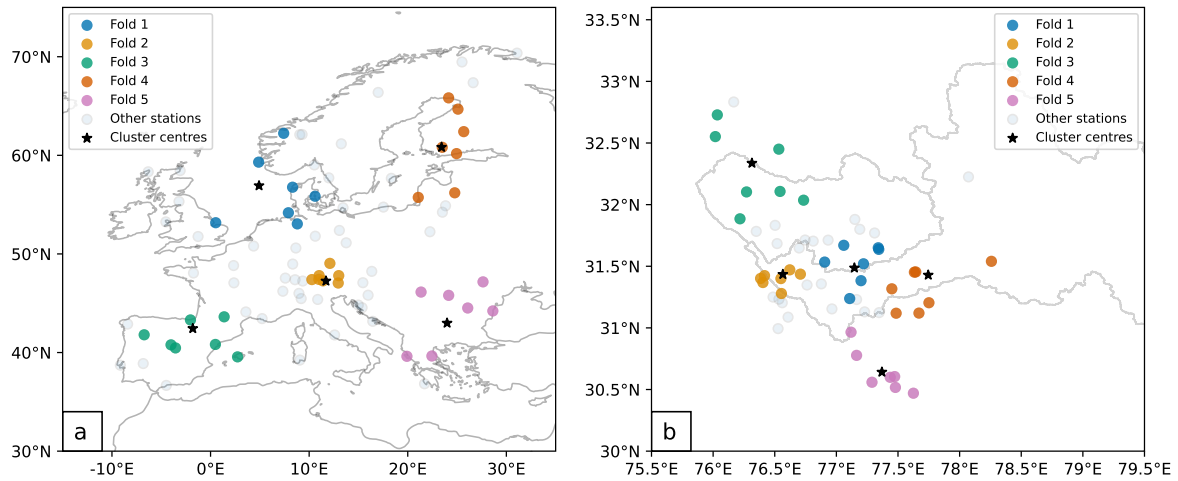


**Figure 3.** Maps of cross-validation folds over a) Europe and b) the Upper-upper Beas and Sutelj Basins-basins. The round marker represent the stations, the marker colours the different folds, and the stars the cluster centres found via k-means. The coastlines are plotted in black in (a) and the Upper-upper Beas and Sutelj Basins-basins watershed boundaries in light grey in (b).

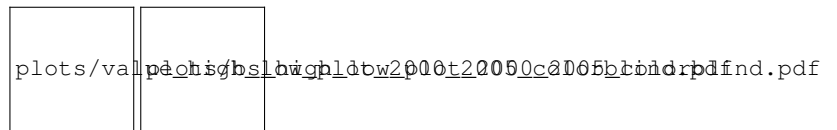


**Figure 4.** MFGP high-fidelity-high-fidelity  $R^2$  as a function low-fidelity-low-fidelity  $R^2$  over a) ‘data-sparse’ Europe and b) Upper-upper Beas and Sutelj Basins-basins. The colours correspond to the folds shown in Figure 3. Values above the dashed line show an improvement over the low-fidelity-low-fidelity MFGP fit. The plots shows that as the low-fidelity-low-fidelity  $R^2$  decreases the high-fidelity-high-fidelity  $R^2$  stays relatively high. This illustrates that important gains can be made over using ERA5 alone.

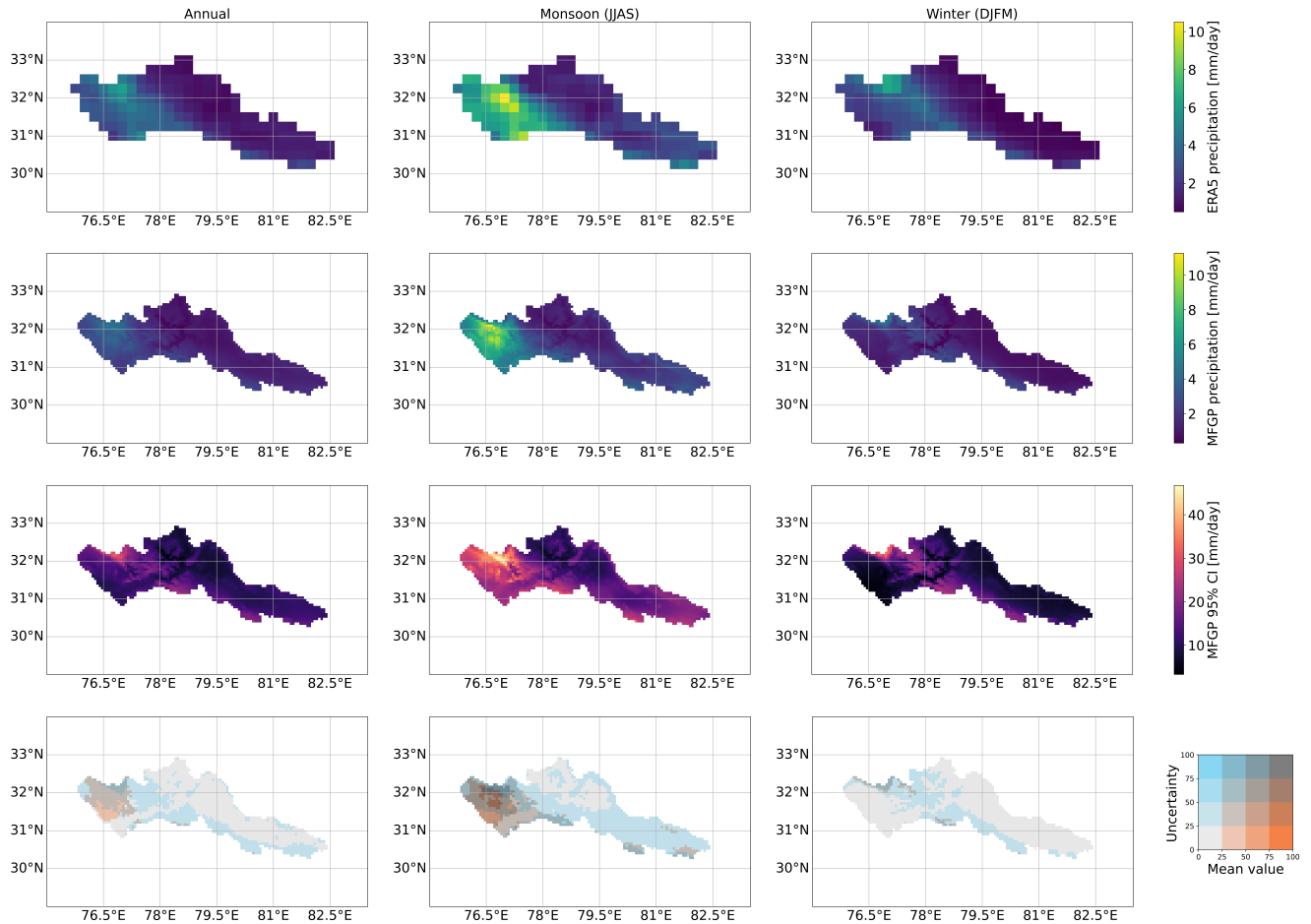


**Figure 5.** Spatial distribution of average precipitation from 2000 to 2009 over the Upper-upper Beas and Sutlej Basins-basins from ERA5 (top row), the MFGP model-posterior mean (second row), the MFGP model-95% confidence interval (third row), and bivariate chloropleth map of the MFGP posterior mean and 95% confidence interval (bottom row). Here the 95% confidence interval is used as the measure of uncertainty. Results are shown for annual (first column), summer (JJAS; second column) and winter (DJFM; third column).

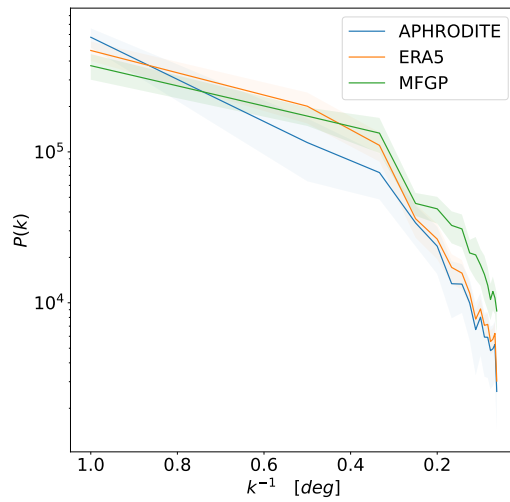


**Figure 6.** Power spectrum densities of the MFGP model, ERA5 and APHRODITE over a  $2^\circ$  by  $2^\circ$  area ( $31^\circ$ - $33^\circ$ N,  $77^\circ$ - $79^\circ$ E) between 2000-2009. ERA5 and APHRODITE data are linearly interpolated to the same resolution as the MFGP output. The y-axis shows the power spectrum spectral density as a function of resolution, i.e. the inverse of the wavenumber  $k$ . The continuous lines show the average power spectrum spectral densities and the shaded areas represent their standard deviation over time. All three datasets are z-scored prior to the analysis.

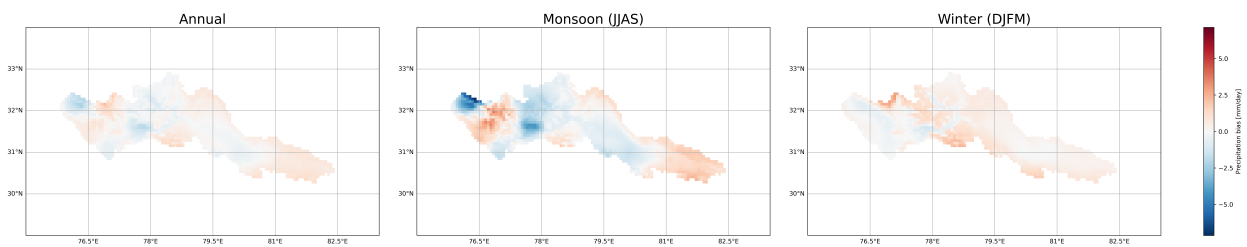


**Figure 7.** APHRODITE - MFGP differences between 2000 and 2009 over the Upper upper Beas and Sutlej Basins basins. Columns represent outputs for annual, monsoon (JJAS), and winter (DJFM) averages respectively.



## Appendix A: More Bayesian inference

### A1 Learning Gaussian Process hyperparameters

For multiple input-output pairs,  $\mathbf{X}$  and  $\mathbf{Y}$ , the logarithm of the marginal likelihood is calculated. This is defined as the probability density of the observations given the hyperparameters:

$$560 \quad \log(p(\mathbf{Y}|\mathbf{X}, \boldsymbol{\theta})) = -\frac{1}{2}(\mathbf{Y} - \boldsymbol{\mu})^T(\mathbf{K} + \sigma_n^2\mathbf{I})^{-1}(\mathbf{Y} - \boldsymbol{\mu}) - \frac{1}{2}\log(|\mathbf{K} + \sigma_n^2\mathbf{I}|) - \frac{N}{2}\log(2\pi) \quad (\text{A1})$$

where  $\mathbf{K}$  is the covariance matrix constructed from the kernel function  $k$ ,  $\sigma_n$  is the noise specified at the observations. The logarithm of the likelihood is used to simplify the differentiation during Maximum Likelihood Estimation of the hyperparameters.

### A2 Predicting with Gaussian Processes

565 Assuming a Gaussian likelihood for  $\epsilon$  (see Equation 1), calculating the posterior distribution  $p(f_*|\mathbf{Y}, \mathbf{X})$  is tractable and can be used to perform predictive inference for a new outputs  $f_*$ , given a new inputs  $\mathbf{X}_*$  as:

$$p(f_*|\mathbf{Y}, \mathbf{X}, \mathbf{X}_*) = \mathcal{N}(f_*|\mu_*(\mathbf{X}_*), \sigma_*^2(\mathbf{X}_*)) \quad (\text{A2})$$

### A3 **Predicting with Gaussian Processes**

570 Predictions are computed using the posterior mean  $\mu_*$ , while the uncertainty associated with these predictions is quantified through the posterior variance  $\sigma_*^2$ :

$$\mu_*(\mathbf{X}_*) = \mathbf{k}_{*n_*N}(\mathbf{K} + \sigma_n^2\mathbf{I})^{-1}\mathbf{Y} \quad (\text{A3})$$

$$\sigma_*^2(\mathbf{X}_*) = \mathbf{k}_{**} - \mathbf{k}_{*n_*N}(\mathbf{K} + \sigma_n^2\mathbf{I})^{-1}\mathbf{k}_{*n_*N}^T \quad (\text{A4})$$

where  $\mathbf{k}_{*n} = [k(\mathbf{x}_*, \mathbf{x}_1), \dots, k(\mathbf{x}_*, \mathbf{x}_n)]$  and  $\mathbf{k}_{**} = k(\mathbf{x}_*, \mathbf{x}_*)\mathbf{k}_{*N} = k(\mathbf{X}_*, \mathbf{X})$  and  $\mathbf{k}_{**} = k(\mathbf{X}_*, \mathbf{X}_*)$ . In other words, the variance captures how much uncertainty remains after seeing the data.

### 575 A3 MFGP inference

At each level of the MFGP, the predicted mean  ~~$\mu_t$  and variance  $\sigma_t^2$~~   $\mu_t$  and variance  $\sigma_t^2$  are given by:

$$\mu_t(\mathbf{X}_*) = \rho_t\mu_{t-1}(\mathbf{X}_*) + \mu_{\text{err}} + \mathbf{k}_{*n_tN_t}\mathbf{K}_t^{-1}[\mathbf{Y}_t - \rho_t\mu_{t-1}(\mathbf{X}_t) - \mu_{\text{err}}] \quad (\text{A5})$$

$$\sigma_t^2(\mathbf{X}_*) = \rho_t^2\sigma_{t-1}^2(\mathbf{X}_*) + \mathbf{k}_{**} - \mathbf{k}_{*n_tN_t}\mathbf{K}_t^{-1}\mathbf{k}_{*n_tN_t}^T \quad (\text{A6})$$

580 where  $\mathbf{X}_*$  is a set of test points used over the domain of interest and  $n_tN_t$  denotes the number of training point locations where we have observed data from the  $t$ -th information source. The mean and the uncertainty are thus elegantly propagated

from one fidelity layer to the next. As the sum of two GPs is another GP, we can also write out the ~~linear~~-MFGP model as:

$$\begin{bmatrix} f_{t-1} \\ f_t \end{bmatrix} \sim GP \left( \begin{bmatrix} \mu_{t-1} \\ \mu_t \end{bmatrix} \begin{bmatrix} k_{t-1} & \rho_t k_{t-1} \\ \rho_t k_{t-1} & \rho_t^2 k_{t-1} + k_{\text{err}} \end{bmatrix} \right) \quad (\text{A7})$$

## Appendix B: Metric definitions

### B1 Root mean square error (RMSE)

585 The RMSE represents the typical distance of the model from the data. It is given by:

$$\text{RMSE} = \sqrt{\langle (y_i - f_i)^2 \rangle} \quad (\text{B1})$$

where  $y_i$  is the observed value and  $f_i$  the predicted value. We use  $\langle \rangle$  here and in the following definitions as a shorthand for the mean. The RMSE is sensitive to outliers and systematic errors. The ~~5th and 95th~~ 5th and 95th percentile RMSE values are calculated by computing the RMSE for the ~~high-fidelity~~ high-fidelity data points in the ~~5th and 95th~~ 5th and 95th percentiles respectively.

### B2 Coefficient of determination ( $R^2$ )

The  $R^2$  represents the percentage of the data variance that can be explained by the model. It is given by:

$$R^2 = 1 - \frac{\text{SS}_{\text{res}}}{\text{SS}_{\text{tot}}} = 1 - \frac{\sum_i (y_i - f_i)^2}{\sum_i (y_i - \bar{y})^2} \quad (\text{B2})$$

where  $\text{SS}_{\text{res}}$  is the sum of the squared residuals and  $\text{SS}_{\text{tot}}$  the total sum of squares. An  $R^2$  of 1 indicates a perfect fit whilst a negative  $R^2$  means the model performs worse than the mean. Although negative  $R^2$  scores are unlikely in interpolation settings, they are possible when making predictions outside of the training distribution.

### B3 Mean log loss (MLL)

Using the predictive distribution at each test input, the probability of the target given the model can be calculated. The log loss (Rasmussen et al., 2006) is given by taking the negative logarithm of this probability. Taking the mean over all inputs gives the mean log loss (MLL):

$$\text{MLL} = -\langle \log p(y_* | \boldsymbol{\theta}, \mathbf{x}_*) \rangle = \left\langle \frac{1}{2} \log(2\pi\sigma_*^2) + \frac{(y_* - \bar{f}(\mathbf{x}_*))^2}{2\sigma_*^2} \right\rangle \quad (\text{B3})$$

where  $\bar{f}(\mathbf{x}_*)$  is the model's posterior mean,  $\sigma_*^2$  the model's variance  $\boldsymbol{\theta}$  are the model's optimised hyperparameters, and  $y_*$  denotes the target at test points, value, all at test point  $\mathbf{x}_*$  denotes the test point and  $\bar{f}(\mathbf{x}_*)$  denotes the mean prediction. Smaller values imply more skill. The MLL is calculated prior to the inverse Box-Cox transformation, as this metric assumes the model output is Gaussian.

## Appendix C: Further data analysis

610 [This appendix brings together more analysis around the validation experiments. More specifically, Table C1 compares observational data over Europe and the upper Beas and Sutlej basins and their optimised GP hyperparameters. Overall this breakdown shows that the distribution of precipitation over the upper Beas and Sutlej basins is more complicated than that over Europe despite a similar standardised gauge density/GP lengthscales between gauges.](#)

Metric	mean	std dev	5 <sup>th</sup> percent	95 <sup>th</sup> percent	GP $l_{lon}$		GP $l_{lat}$	
Unit	[mm/day]	[mm/day]	[mm/day]	[mm/day]	[°E]	z-scored	[°N]	z-scored
VALUE gauges	2.39	2.19	0.22	6.61	4.96	0.47	3.80	0.49
BS gauges	2.95	3.98	0.00	11.17	0.26	0.52	0.23	0.48

**Table C1.** Precipitation statistics over Europe and the Beas and Sutlej using gauge data from 2000 to 2005. The mean, standard deviation, the 5<sup>th</sup> and 95<sup>th</sup> percentile values, and lengthscale values for the datasets are presented. The lengthscales are calculated by fitting a GP with a Matérn  $\frac{5}{2}$  kernel to each of the gauge datasets with time, latitude, longitude and elevation as inputs.

[Table C2 shows the performance of the benchmark datasets for the upper Beas and Sutlej validation experiment. These results are not directly comparable to the MFGP model as the data used to create these products are or are likely included in the held out validation sets. They can however give us a indication of how well these models perform in absolute terms for this gauged area.](#)

	Input features	RMSE [mm/day]	RMSE5 [mm/day]	RMSE95 [mm/day]	R <sup>2</sup>
ERA5	multiple <sup>†</sup>	3.03±1.05	0.53±0.58	6.01±3.52	-0.30±2.18
APHRODITE	gauges	<b>2.27±0.92</b>	<b>0.27±0.30</b>	<b>5.35±3.26</b>	<b>0.45±0.68</b>
TRMM	remote sensing	3.83±1.36	0.58±0.77	8.18±4.27	-0.22±0.68
CRU TS	gauges	2.87±1.20	0.43±0.24	7.59±4.71	0.19±1.22
Bias-corrected WRF	gauges + WRF	3.12±1.00	0.37±0.72	7.02±4.21	-0.10±1.77

**Table C2.** RMSE and R<sup>2</sup> values for benchmark datasets over the Upper Beas and Sutlej Basins between 2000 and 2005 for cross-validation test stations. The errors represent the standard deviation across the cross validation folds. Bolded values show the best model performance for a given metric. <sup>†</sup> ERA5 uses only remote sensing data for precipitation measurements but is also constrained using direct measurements for other climatic variables.

## 615 Appendix D: MFGP time sensitivity

The computational complexity of the MFGP framework only allows the modeller to train over climatically short periods of time. In this study, we assume that long term variability is accurately captured by ERA5 and that there is limited information to learn by training over longer time periods. This assumption is tested in the following experiment where we repeat the ‘data-sparse’ version of the European validation experiment over different time ranges. Figure D1 shows the model performance as  
620 a function of the number of time points for the different folds. ~~Asides~~ Aside from a dip at the 2 year mark, there is no ~~visible~~ generalised trend change between different time periods across folds.

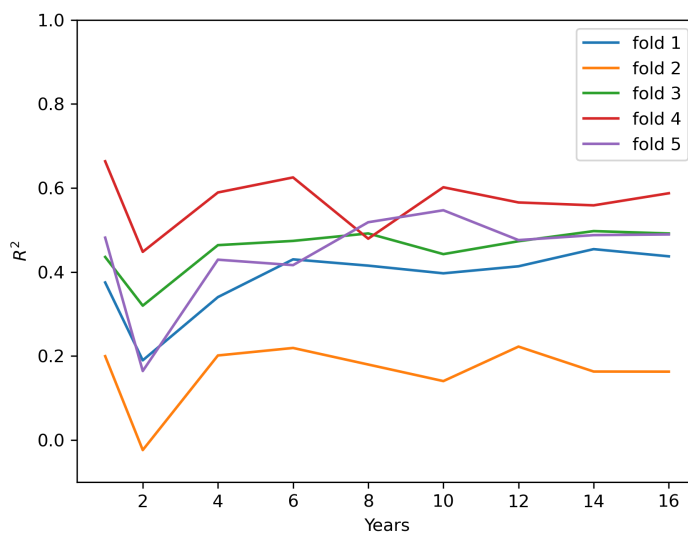


**Figure D1.**  $R^2$  as function of years used to model the data across the different folds of the ‘data-sparse’ experiment over Europe.

## Appendix E: Machine learning baseline results

625 To contextualise the performance of the MFGP models linear interpolation and downscaling using random forests and support vector regression. The models are applied to the validation experiments presented in Section 4. These models have no explicit way of merging multiple data sources, instead we use ERA5 as a fifth input to models. The random forest models were trained with 100 trees and the stopping tolerance for the support vector regression model was set to  $10^{-3}$ . We note that no systematic hyperparameter search was performed for these models.

630 We also compare the MFGP to a Convolutional Conditional Neural Process (ConvCNP). In this setup, we used the high-fidelity elevation as a context dataset to the model. The model itself was trained using a U-Net with four downsampling layers each with 64 channels, an internal density of 500 and a learning rate of  $5 \times 10^{-5}$  and sampling all the data at each timestep to create the training tasks. The models are trained for 20 and 15 epochs for the Europe and Beas-Sutlej experiments respectively. Again no systematic hyperparameter search or tailored sampling approach was performed for the ConvCNP models.

Model	Training features	RMSE [mm/day]	RMSE5 [mm/day]	RMSE95 [mm/day]	R <sup>2</sup>	MLL
Linear reg.	ERA5	1.72±0.46	1.75±0.18	5.21±1.55	0.04±0.06	-
RF	ERA5 + gauges	1.12±0.44	<b>0.45±0.19</b>	<b>2.62±0.93</b>	0.61±0.09	-
SVR <sub>RBF</sub>	ERA5 + gauges	1.14±0.46	0.53±0.33	3.03±1.48	0.60±0.12	-
MFGP	ERA5 + gauges	<b>1.06±0.42</b>	0.51±0.20	2.72±1.54	<b>0.65±0.09</b>	<b>0.89±0.20</b>
ConvCNP	ERA5 + gauges	2.16±0.76	2.29±0.93	4.25±1.60	-0.49±0.48	2.40±0.91

**Table E1.** Comparison of model performance metrics trained on ERA5 data for the ‘data-rich’ setup over Europe. We include a linear interpolation model, a random forest (RF), a support vector regression (SVR) model with a smooth Radial Basis Function (RBF) kernel, a ConvCNP and the MFGP model. The metrics include the average RMSE, the 5<sup>th</sup> percentile RMSE (RMSE5), the 95<sup>th</sup> percentile RMSE (RMSE95), the R<sup>2</sup> score, and the MLL. The errors represent the standard deviation across the validation folds.

Model	Training features	RMSE [mm/day]	RMSE5 [mm/day]	RMSE95 [mm/day]	R <sup>2</sup>	MLL
Linear reg.	ERA5	1.77±0.46	1.88±0.25	5.19±1.76	-0.02±0.13	-
RF	ERA5 + gauges	1.16±0.39	<b>0.41±0.20</b>	<b>2.92±1.39</b>	0.57±0.10	-
SVR <sub>RBF</sub>	ERA5 + gauges	1.53±0.62	0.73±0.23	4.64±1.99	0.29±0.19	-
MFGP	ERA5 + gauges	<b>1.13±0.47</b>	0.57±0.23	3.02±1.62	<b>0.62±0.11</b>	<b>0.90±0.20</b>
ConvCNP	ERA5 + gauges	1.92±0.51	1.77±0.78	4.84±1.70	-0.21±0.34	2.36±1.38

**Table E2.** As Table E1 for the ‘data-sparse’ setup over Europe.

Model	Training features	RMSE [mm/day]	RMSE5 [mm/day]	RMSE95 [mm/day]	R <sup>2</sup>	MLL
Linear reg.	ERA5	4.21±0.99	2.21±0.45	14.33±4.03	-0.08±0.05	-
RF	ERA5 + gauges	3.05±1.30	<b>0.52±0.46</b>	9.87±5.47	0.45±0.23	-
SVR <sub>RBF</sub>	ERA5 + gauges	3.36±1.66	0.66±0.38	11.05±6.14	0.34±0.33	-
MFGP	ERA5 + gauges	<b>3.00±0.92</b>	1.66±0.95	<b>9.62±3.63</b>	<b>0.46±0.11</b>	<b>1.79±0.22</b>
ConvCNP	ERA5 + gauges	4.89±0.93	3.57±0.79	14.16±3.85	-0.51±0.32	3.95±0.88

**Table E3.** [As Table E2 for the upper Beas and Sutlej basins.](#)

*Author contributions.* KT designed the experiments, conducted the research, and wrote the manuscript under the supervision of AO, JGH, RET and SH. AO advised on the environmental aspects of the research and analysis. RET and JGH provided feedback on the machine learning experiments and final model design and evaluation. All authors contributed to the manuscript's clarity and coherence and approved the final submitted draft.

*Competing interests.* No competing interest are present.

*Acknowledgements.* This work was supported by the UK Engineering and Physical Sciences Research Council [award number 2270379]. The authors thank Tony Phillips for providing the watershed shapefiles.



## 640 **References**

- Ahmed, K., Iqbal, Z., Khan, N., Rasheed, B., Nawaz, N., Malik, I., and Noor, M.: Quantitative assessment of precipitation changes under CMIP5 RCP scenarios over the northern sub-Himalayan region of Pakistan, *Environment, Development and Sustainability*, 22, 7831–7845, 2020.
- Andermann, C., Bonnet, S., and Gloaguen, R.: Evaluation of precipitation data sets along the Himalayan front, *Geochemistry, Geophysics, Geosystems*, 12, 2011.
- 645 Anders, A. M., Roe, G. H., Hallet, B., Montgomery, D. R., Finnegan, N. J., and Putkonen, J.: Spatial patterns of precipitation and topography in the Himalaya, *Special Paper of the Geological Society of America*, 398, 39–53, 2006.
- Andersson, T. R., Bruinsma, W. P., Markou, S., Requeima, J., Coca-Castro, A., Vaughan, A., Ellis, A.-L., Lazzara, M. A., Jones, D., Hosking, S., et al.: Environmental sensor placement with convolutional Gaussian neural processes, *Environmental Data Science*, 2, e32, 2023.
- 650 Bannister, D., Orr, A., Jain, S. K., Holman, I. P., Momblanch, A., Phillips, T., Adeloje, A. J., Snapir, B., Waive, T. W., Hosking, J. S., et al.: Bias correction of high-resolution regional climate model precipitation output gives the best estimates of precipitation in Himalayan catchments, *Journal of Geophysical Research: Atmospheres*, 124, 14 220–14 239, 2019.
- Baño-Medina, J., Manzanar, R., and Gutiérrez, J. M.: Configuration and intercomparison of deep learning neural models for statistical downscaling, *Geoscientific Model Development*, 13, 2109–2124, 2020.
- 655 Bhardwaj, A., Ziegler, A. D., Wasson, R. J., and Chow, W. T.: Accuracy of rainfall estimates at high altitude in the Garhwal Himalaya (India): A comparison of secondary precipitation products and station rainfall measurements, *Atmospheric Research*, 188, 30–38, 2017.
- Bookhagen, B. and Burbank, D. W.: Topography, relief, and TRMM-derived rainfall variations along the Himalaya, *Geophysical Research Letters*, 33, 2006.
- Bookhagen, B. and Burbank, D. W.: Toward a complete Himalayan hydrological budget: Spatiotemporal distribution of snowmelt and rainfall and their impact on river discharge, *Journal of Geophysical Research: Earth Surface*, 115, 2010.
- 660 Bui, T. D., Nguyen, C., and Turner, R. E.: Streaming sparse Gaussian process approximations, *Advances in Neural Information Processing Systems*, 30, 2017.
- Cannon, F., Carvalho, L. M., Jones, C., Hoell, A., Norris, J., Kiladis, G. N., and Tahir, A. A.: The influence of tropical forcing on extreme winter precipitation in the western Himalaya, *Climate Dynamics*, 48, 1213–1232, 2017.
- 665 Chen, Y., Sharma, S., Zhou, X., Yang, K., Li, X., Niu, X., Hu, X., and Khadka, N.: Spatial performance of multiple reanalysis precipitation datasets on the southern slope of central Himalaya, *Atmospheric Research*, 250, 105 365, 2021.
- Collier, E. and Immerzeel, W. W.: High-resolution modeling of atmospheric dynamics in the Nepalese Himalaya, *Journal of Geophysical Research: Atmospheres*, 120, 9882–9896, 2015.
- Cutajar, K., Pullin, M., Damianou, A., Lawrence, N., and González, J.: Deep gaussian processes for multi-fidelity modeling, *arXiv preprint arXiv:1903.07320*, 2019.
- 670 Dahri, Z. H., Ludwig, F., Moors, E., Ahmad, B., Khan, A., and Kabat, P.: An appraisal of precipitation distribution in the high-altitude catchments of the Indus basin, *Science of the Total Environment*, 548, 289–306, 2016.
- Dahri, Z. H., Ludwig, F., Moors, E., Ahmad, S., Ahmad, B., Ahmad, S., Riaz, M., and Kabat, P.: Climate change and hydrological regime of the high-altitude Indus basin under extreme climate scenarios, *Science of the Total Environment*, 768, 144 467, 2021a.
- 675 Dahri, Z. H., Ludwig, F., Moors, E., Ahmad, S., Ahmad, B., Shoaib, M., Ali, I., Iqbal, M. S., Pomee, M. S., Mangrio, A. G., et al.: Spatio-temporal evaluation of gridded precipitation products for the high-altitude Indus basin, *International Journal of Climatology*, 41, 4283–4306, 2021b.

- Danielson, J. J. and Gesch, D. B.: Global multi-resolution terrain elevation data 2010 (GMTED2010), 2011.
- 680 Daulton, S., Balandat, M., and Bakshy, E.: Differentiable expected hypervolume improvement for parallel multi-objective Bayesian optimization, *Advances in Neural Information Processing Systems*, 33, 9851–9864, 2020.
- Daulton, S., Balandat, M., and Bakshy, E.: Parallel bayesian optimization of multiple noisy objectives with expected hypervolume improvement, *Advances in Neural Information Processing Systems*, 34, 2187–2200, 2021.
- Dee, D. P., Uppala, S. M., Simmons, A. J., Berrisford, P., Poli, P., Kobayashi, S., Andrae, U., Balmaseda, M., Balsamo, G., Bauer, d. P., et al.: The ERA-Interim reanalysis: Configuration and performance of the data assimilation system, *Quarterly Journal of the royal meteorological society*, 137, 553–597, 2011.
- 685 Dimri, A.: Bias correction demonstration in two of the Indian Himalayan river basins, *Journal of Water and Climate Change*, 12, 1297–1309, 2021.
- Dimri, A., Niyogi, D., Barros, A., Ridley, J., Mohanty, U., Yasunari, T., and Sikka, D.: Western disturbances: a review, *Reviews of Geophysics*, 53, 225–246, 2015.
- 690 Drucker, H., Burges, C. J., Kaufman, L., Smola, A., and Vapnik, V.: Support vector regression machines, *Advances in neural information processing systems*, 9, 1996.
- Duan, K., Xu, B., and Wu, G.: Snow accumulation variability at altitude of 7010 m asl in Muztag Ata Mountain in Pamir Plateau during 1958–2002, *Journal of Hydrology*, 531, 912–918, 2015.
- Duvenaud, D., Lloyd, J., Grosse, R., Tenenbaum, J., and Zoubin, G.: Structure discovery in nonparametric regression through compositional kernel search, in: *International Conference on Machine Learning*, pp. 1166–1174, PMLR, 2013.
- 695 Gerlitz, L., Conrad, O., and Böhner, J.: Large scale atmospheric forcing and topographic modification of precipitation rates over High Asia—a neural network based approach, *Earth Syst Dyn Discussions*, 5, 1275–1317, 2014.
- Gordon, J., Bruinsma, W. P., Foong, A. Y., Requeima, J., Dubois, Y., and Turner, R. E.: Convolutional conditional neural processes, *arXiv preprint arXiv:1910.13556*, 2019.
- 700 Gutiérrez, J. M., Maraun, D., Widmann, M., Huth, R., Hertig, E., Benestad, R., Rössler, O., Wibig, J., Wilcke, R., Kotlarski, S., et al.: An intercomparison of a large ensemble of statistical downscaling methods over Europe: Results from the VALUE perfect predictor cross-validation experiment, *International journal of climatology*, 39, 3750–3785, 2019.
- Harris, I., Osborn, T. J., Jones, P., and Lister, D.: Version 4 of the CRU TS monthly high-resolution gridded multivariate climate dataset, *Scientific data*, 7, 109, 2020.
- 705 Hawkins, E. and Sutton, R.: The potential to narrow uncertainty in regional climate predictions, *Bulletin of the American Meteorological Society*, 90, 1095–1108, 2009.
- Hersbach, H., Bell, B., Berrisford, P., Hirahara, S., Horányi, A., Muñoz-Sabater, J., Nicolas, J., Peubey, C., Radu, R., Schepers, D., et al.: The ERA5 global reanalysis, *Quarterly Journal of the Royal Meteorological Society*, 146, 1999–2049, 2020.
- Ho, T. K.: Random decision forests, in: *Proceedings of 3rd international conference on document analysis and recognition*, vol. 1, pp. 278–282, IEEE, 1995.
- 710 Hussain, S., Song, X., Ren, G., Hussain, I., Han, D., and Zaman, M.: Evaluation of gridded precipitation data in the Hindu Kush–Karakoram–Himalaya mountainous area, *Hydrological sciences journal*, 62, 2393–2405, 2017.
- Immerzeel, W., Wanders, N., Lutz, A., Shea, J., and Bierkens, M.: Reconciling high-altitude precipitation in the upper Indus basin with glacier mass balances and runoff, *Hydrology and Earth System Sciences*, 19, 4673–4687, 2015.

- 715 Immerzeel, W. W., Lutz, A. F., Andrade, M., Bahl, A., Biemans, H., Bolch, T., Hyde, S., Brumby, S., Davies, B., Elmore, A., et al.: Importance and vulnerability of the world's water towers, *Nature*, 577, 364–369, 2020.
- Japan Aerospace Exploration Agency: GPM Data Utilization Handbook, Tech. rep., Japan Aerospace Exploration Agency, 2018.
- Ji, X., Li, Y., Luo, X., He, D., Guo, R., Wang, J., Bai, Y., Yue, C., and Liu, C.: Evaluation of bias correction methods for APHRODITE data to improve hydrologic simulation in a large Himalayan basin, *Atmospheric Research*, 242, 104964, 2020.
- 720 Karki, R., Gerlitz, L., Schickhoff, U., Scholten, T., Böhner, J., et al.: Quantifying the added value of convection-permitting climate simulations in complex terrain: a systematic evaluation of WRF over the Himalayas, *Earth System Dynamics*, 8, 507–528, 2017.
- King, A. D., Alexander, L. V., and Donat, M. G.: The efficacy of using gridded data to examine extreme rainfall characteristics: a case study for Australia, *International Journal of Climatology*, 33, 2376–2387, 2013.
- Krishnan, R., Shrestha, A. B., Ren, G., Rajbhandari, R., Saeed, S., Sanjay, J., Syed, M. A., Vellore, R., Xu, Y., You, Q., et al.: Unravelling  
725 climate change in the Hindu Kush Himalaya: rapid warming in the mountains and increasing extremes, *The Hindu Kush Himalaya assessment: Mountains, climate change, sustainability and people*, pp. 57–97, 2019.
- Kumar, M., Hodnebrog, Ø., Daloz, A. S., Sen, S., Badiger, S., and Krishnaswamy, J.: Measuring precipitation in Eastern Himalaya: Ground validation of eleven satellite, model and gauge interpolated gridded products, *Journal of Hydrology*, 599, 126252, 2021.
- Lalchand, V., Tazi, K., Cheema, T. M., Turner, R. E., and Hosking, S.: Kernel Learning for Explainable Climate Science, in: 16th Bayesian  
730 Modelling Applications Workshop at UAI, 2022.
- Le Gratiet, L. and Garnier, J.: Recursive co-kriging model for design of computer experiments with multiple levels of fidelity, *International Journal for Uncertainty Quantification*, 4, 2014.
- Leander, R. and Buishand, T. A.: Resampling of regional climate model output for the simulation of extreme river flows, *Journal of hydrology*, 332, 487–496, 2007.
- 735 Lederer, A., Conejo, A. J. O., Maier, K. A., Xiao, W., Umlauf, J., and Hirche, S.: Gaussian process-based real-time learning for safety critical applications, in: *International Conference on Machine Learning*, pp. 6055–6064, PMLR, 2021.
- Li, L., Gochis, D. J., Sobolowski, S., and Mesquita, M. D.: Evaluating the present annual water budget of a Himalayan headwater river basin using a high-resolution atmosphere-hydrology model, *Journal of Geophysical Research: Atmospheres*, 122, 4786–4807, 2017.
- Libertino, A., Allamano, P., Laio, F., and Claps, P.: Regional-scale analysis of extreme precipitation from short and fragmented records,  
740 *Advances in Water Resources*, 112, 147–159, 2018.
- Liu, H., Ong, Y.-S., Shen, X., and Cai, J.: When Gaussian process meets big data: A review of scalable GPs, *IEEE transactions on neural networks and learning systems*, 31, 4405–4423, 2020.
- Lund, J., Forster, R. R., Rupper, S. B., Deeb, E. J., Marshall, H., Hashmi, M. Z., and Burgess, E.: Mapping snowmelt progression in the Upper Indus Basin with synthetic aperture radar, *Frontiers in Earth Science*, p. 318, 2020.
- 745 Lyu, Y. and Yong, B.: A novel Double Machine Learning strategy for producing high-precision multi-source merging precipitation estimates over the Tibetan Plateau, *Water Resources Research*, 60, e2023WR035643, 2024.
- MacKay, D. J. C.: Bayesian non-linear modelling for the prediction competition, *ASHRAE Transactions*, 100, 1053–1062, 1994.
- Maraun, D. and Widmann, M.: *Statistical downscaling and bias correction for climate research*, Cambridge University Press, 2018.
- Markou, S., Requeima, J., Bruinsma, W., Vaughan, A., and Turner, R. E.: Practical Conditional Neural Process Via Tractable Dependent  
750 Predictions, in: *International Conference on Learning Representations*, 2022.
- Maussion, F., Scherer, D., Mölg, T., Collier, E., Curio, J., and Finkelnburg, R.: Precipitation seasonality and variability over the Tibetan Plateau as resolved by the High Asia Reanalysis, *Journal of Climate*, 27, 1910–1927, 2014.

- Mei, Y., Maggioni, V., Houser, P., Xue, Y., and Rouf, T.: A nonparametric statistical technique for spatial downscaling of precipitation over High Mountain Asia, *Water Resources Research*, 56, e2020WR027472, 2020.
- 755 Meng, J., Li, L., Hao, Z., Wang, J., and Shao, Q.: Suitability of TRMM satellite rainfall in driving a distributed hydrological model in the source region of Yellow River, *Journal of Hydrology*, 509, 320–332, 2014.
- Muñoz-Sabater, J., Dutra, E., Agustí-Panareda, A., Albergel, C., Arduini, G., Balsamo, G., Boussetta, S., Choulga, M., Harrigan, S., Hersbach, H., et al.: ERA5-Land: A state-of-the-art global reanalysis dataset for land applications, *Earth system science data*, 13, 4349–4383, 2021.
- 760 Ning, C., Wang, Y., Nan, Z., Chen, H., and Liu, C.: Study on correction of daily precipitation data of the Qinghai-Tibetan plateau with machine learning models, in: 2016 IEEE International Geoscience and Remote Sensing Symposium (IGARSS), pp. 517–520, IEEE, 2016.
- Norris, J., Carvalho, L. M., Jones, C., Cannon, F., Bookhagen, B., Palazzi, E., and Tahir, A. A.: The spatiotemporal variability of precipitation over the Himalaya: evaluation of one-year WRF model simulation, *Climate Dynamics*, 49, 2179–2204, 2017.
- 765 Norris, J., Carvalho, L. M., Jones, C., and Cannon, F.: Deciphering the contrasting climatic trends between the central Himalaya and Karakoram with 36 years of WRF simulations, *Climate Dynamics*, 52, 159–180, 2019.
- Norris, J., Carvalho, L. M., Jones, C., and Cannon, F.: Warming and drying over the central Himalaya caused by an amplification of local mountain circulation, *Npj Climate and Atmospheric Science*, 3, 1, 2020.
- Orr, A., Listowski, C., Couttet, M., Collier, E., Immerzeel, W., Deb, P., and Bannister, D.: Sensitivity of simulated summer monsoonal precipitation in Langtang Valley, Himalaya, to cloud microphysics schemes in WRF, *Journal of Geophysical Research: Atmospheres*, 122, 6298–6318, 2017.
- Orr, A., Ahmad, B., Alam, U., Appadurai, A., Bharucha, Z. P., Biemans, H., Bolch, T., Chaulagain, N. P., Dhaubanjari, S., Dimri, A., et al.: Knowledge priorities on climate change and water in the Upper Indus Basin: A horizon scanning exercise to identify the top 100 research questions in social and natural sciences, *Earth’s Future*, 10, e2021EF002619, 2022.
- 775 Palazzi, E., Von Hardenberg, J., and Provenzale, A.: Precipitation in the Hindu-Kush Karakoram Himalaya: observations and future scenarios, *Journal of Geophysical Research: Atmospheres*, 118, 85–100, 2013.
- Panday, P. K., Thibeault, J., and Frey, K. E.: Changing temperature and precipitation extremes in the Hindu Kush-Himalayan region: An analysis of CMIP3 and CMIP5 simulations and projections, *International Journal of Climatology*, 35, 3058–3077, 2015.
- Perdikaris, P., Raissi, M., Damianou, A., Lawrence, N. D., and Karniadakis, G. E.: Nonlinear information fusion algorithms for data-efficient multi-fidelity modelling, *Proceedings of the Royal Society A: Mathematical, Physical and Engineering Sciences*, 473, 20160751, 2017.
- 780 Potter, E., Fyffe, C., Orr, A., Quincey, D., Ross, A. N., Rangecroft, S., Medina, K., Burns, H., Llacza, A., Jacome, G., et al.: Projected increases in climate extremes and temperature-induced drought over the Peruvian Andes, 1980–2100, Tech. rep., Copernicus Meetings, 2022.
- Rambali, M.: Policy Analyst, Climate, Biodiversity and Water Division, OECD, personal communication, 2020.
- 785 Rasmussen, C. E., Williams, C. K., et al.: *Gaussian processes for machine learning*, vol. 1, Springer, 2006.
- Remesan, R. and Holman, I. P.: Effect of baseline meteorological data selection on hydrological modelling of climate change scenarios, *Journal of Hydrology*, 528, 631–642, 2015.
- Salzmann, N., Huggel, C., Rohrer, M., and Stoffel, M.: Data and knowledge gaps in glacier, snow and related runoff research—A climate change adaptation perspective, *Journal of Hydrology*, 518, 225–234, 2014.

- 790 Sanjay, J., Krishnan, R., Shrestha, A. B., Rajbhandari, R., and Ren, G.-Y.: Downscaled climate change projections for the Hindu Kush Himalayan region using CORDEX South Asia regional climate models, *Advances in Climate Change Research*, 8, 185–198, 2017.
- Schreiner-McGraw, A. P. and Ajami, H.: Combined impacts of uncertainty in precipitation and air temperature on simulated mountain system recharge from an integrated hydrologic model, *Hydrology and Earth System Sciences*, 26, 1145–1164, 2022.
- 795 Shukla, A. K., Ojha, C. S. P., Singh, R. P., Pal, L., and Fu, D.: Evaluation of TRMM precipitation dataset over Himalayan catchment: the upper Ganga basin, India, *Water*, 11, 613, 2019.
- Sigdel, M. and Ma, Y.: Variability and trends in daily precipitation extremes on the northern and southern slopes of the central Himalaya, *Theoretical and Applied Climatology*, 130, 571–581, 2017.
- Singh, D., Sharma, V., and Juyal, V.: Observed linear trend in few surface weather elements over the Northwest Himalayas (NWH) during winter season, *Journal of Earth System Science*, 124, 553–565, 2015.
- 800 Skamarock, W. C., Klemp, J. B., Dudhia, J., Gill, D. O., Barker, D. M., Duda, M. G., Huang, X.-Y., Wang, W., Powers, J. G., et al.: A description of the advanced research WRF version 3, NCAR technical note, 475, 113, 2008.
- Sun, H., Yao, T., Su, F., He, Z., Tang, G., Li, N., Zheng, B., Huang, J., Meng, F., Ou, T., et al.: Corrected ERA5 precipitation by machine learning significantly improved flow simulations for the third pole basins, *Journal of Hydrometeorology*, 23, 1663–1679, 2022.
- Tazi, K.: Downscaled ERA5 monthly precipitation data using Multi-Fidelity Gaussian Processes between 1980 and 2012 for the Upper Beas and Sutlej Basins, Himalayas, <https://doi.org/10.5285/b2099787-b57c-44ae-bf42-0d46d9ec87cc>, 2023.
- 805 Tazi, K., Lin, J. A., Viljoen, R., Gardner, A., John, S., Ge, H., and Turner, R. E.: Beyond Intuition, a Framework for Applying GPs to Real-World Data, in: ICML Workshop on Structured Probabilistic Inference and Generative Modeling, 2023.
- Titsias, M.: Variational learning of inducing variables in sparse Gaussian processes, in: *Artificial intelligence and statistics*, pp. 567–574, PMLR, 2009.
- 810 Tresp, V.: A Bayesian committee machine, *Neural computation*, 12, 2719–2741, 2000.
- TROPOMI, T. M. I. T.: GMTED2010 elevation data at different resolutions, Tropospheric Emission Monitoring Internet Service, Royal Netherlands Meteorological Institute, <https://www.temis.nl/data/gmted2010/index.php>, 2019.
- Vaughan, A., Tebbutt, W., Hosking, J. S., and Turner, R. E.: Convolutional conditional neural processes for local climate downscaling, *Geoscientific Model Development*, 15, 251–268, 2022.
- 815 Wester, P., Mishra, A., Mukherji, A., and Shrestha, A. B.: The Hindu Kush Himalaya assessment: mountains, climate change, sustainability and people, Springer Nature, 2019.
- Wilson, A. and Nickisch, H.: Kernel interpolation for scalable structured Gaussian processes (KISS-GP), in: *International Conference on Machine Learning*, pp. 1775–1784, PMLR, 2015.
- Winiger, M., Gumpert, M., and Yamout, H.: Karakorum–Hindukush–western Himalaya: assessing high-altitude water resources, *Hydrological Processes: An International Journal*, 19, 2329–2338, 2005.
- 820 Wulf, H., Bookhagen, B., and Scherler, D.: Differentiating between rain, snow, and glacier contributions to river discharge in the western Himalaya using remote-sensing data and distributed hydrological modeling, *Advances in Water Resources*, 88, 152–169, 2016.
- Xiang, Y., Zeng, C., Zhang, F., and Wang, L.: Effects of climate change on runoff in a representative Himalayan basin assessed through optimal integration of multi-source precipitation data, *Journal of Hydrology: Regional Studies*, 53, 101 828, 2024.
- 825 Yadav, B. C., Thayyen, R. J., Jain, K., and Dimri, A. P.: Himalayan Re-gridded and Observational Experiment (HiROX): Part I–Development, *Journal of Earth System Science*, 133, 22, 2024.

- Yan, Y., Wang, H., Li, G., Xia, J., Ge, F., Zeng, Q., Ren, X., and Tan, L.: Projection of future extreme precipitation in China based on the CMIP6 from a machine learning perspective, *Remote Sensing*, 14, 4033, 2022.
- 830 Yatagai, A., Kamiguchi, K., Arakawa, O., Hamada, A., Yasutomi, N., and Kitoh, A.: APHRODITE: Constructing a long-term daily gridded precipitation dataset for Asia based on a dense network of rain gauges, *Bulletin of the American Meteorological Society*, 93, 1401–1415, 2012.
- Yin, Z.-Y., Zhang, X., Liu, X., Colella, M., and Chen, X.: An assessment of the biases of satellite rainfall estimates over the Tibetan Plateau and correction methods based on topographic analysis, *Journal of Hydrometeorology*, 9, 301–326, 2008.
- 835 Zhang, L., Li, X., Zheng, D., Zhang, K., Ma, Q., Zhao, Y., and Ge, Y.: Merging multiple satellite-based precipitation products and gauge observations using a novel double machine learning approach, *Journal of Hydrology*, 594, 125 969, 2021.